QUARTERLY JOURNAL OF THE ROYAL METEOROLOGICAL SOCIETY
Q. J. R. Meteorol. Soc. **134**: 317–335 (2008)
DOI: 10.1002/qj.203

Scaling turbulent atmospheric stratification. III: Space–time stratification of passive scalars from lidar data

A. Radkevich,[a,g] S. Lovejoy,[a,e]* K. B. Strawbridge,[b] D. Schertzer[c,f] and M. Lilley[a,d]
[a] *Department of Physics, McGill University, Montreal, Canada*
[b] *Centre for Atmospheric Research Experiments, Science and Technology Branch, Environment Canada, Egbert, Canada*
[c] *CEREVE, Ecole Nationale des Ponts et Chaussées, Marne-la-Vallée, France*
[d] *GreCo, Institut d'Astrophysique de Paris, 98bis Boulevard Arago, 75014 Paris, France*
[e] *Centre GEOTOP UQAM/McGill, Université du Québec, Montréal, Canada*
[f] *Météo France, 1 Quai Branly, Paris 75007, France*
[g] *Candian Centre for Remote Sensing, 588 Booth Street, Ottawa, Ontario, Canada*

ABSTRACT: In this third and final part of the series, we concentrate on the temporal behaviour of atmospheric passive scalars. We first recall that – although the full (x, y, z, t) turbulent processes respect an anisotropic scale invariance – that due to advection – the generator will generally not be a diagonal matrix. This implies that the scaling of (1-D) temporal series will generally involve three exponents in real space: 1/3, 1/2, 3/5, for spectra $\beta_\tau = 5/3$, 2, 11/5, with the first and last corresponding to domination by advection (horizontal and vertical respectively), and the second to pure temporal development (no advection). We survey the literature and find that almost all the empirical β_τ values are indeed in the range 5/3 to 2. We then use meteorological analyses to argue that, although pure temporal development is unlikely to be dominant for time-scales less than the eddy turnover time of the largest structures (about 2 weeks), an intermittent vertical velocity could quite easily explain the occasionally observed $\beta_\tau \approx 2$ spectra.

We then use state-of-the-art vertically pointing lidar data of backscatter ratios from both aerosols and cirrus clouds yielding several (z, t) vertical space–time cross-sections with resolution of 3.75 m in the vertical, 0.5–30 s in time and spanning 3–4 orders of magnitude in temporal scale. We first test the predictions of the anisotropic, multifractal extension of the Corrsin-Obukhov law in the vertical and in time, separately finding that the cirrus and aerosol backscatters both followed the theoretical (anisotropic) scalings accurately; three of the six cases show dominance by the horizontal wind, the others by the vertical wind. In order to test the theory in arbitrary directions in this (z, t) space, and in order to get more complete information about the underlying physical scale, we develop and apply a new Anisotropic Scaling Analysis Technique (ASAT) which is based on a nonlinear space–time coordinate transformation. This transforms the original differential scaling into standard self-similar scaling; there remains only a 'trivial' anisotropy. This method is used in real space on 2-D structure functions. It is applied to both the new (z, t) data as well as the (x, z) data discussed in part II. Using ASAT, we verify the theory to within about 10% over more than three orders of magnitude of space–time scales in arbitrary directions in (x, z) and (z, t) spaces. By considering the high- (and low-) order structure functions, we verify the theory for both weak and strong structures; as predicted, their average anisotropies are apparently the same.

Putting together the results for (x, z) and (z, t), and assuming that there is no overall stratification in the horizontal (x, y) plane, we find that the overall (x, y, z, t) space is found to have an effective 'elliptical dimension' characterizing the overall space–time stratification equal to $D_{\mathrm{eff,st}} = 3.21 \pm 0.05$.

KEY WORDS fractal; multifractal; atmospheric spectrum; lidar; passive scalar

Received 9 December 2005; Revised 10 October 2007; Accepted 23 November 2007

1. Introduction

In parts I (Lovejoy *et al.*, 2008) and II (Lilley *et al.*, 2008), we argued that an anisotropic multifractal extension of the classical Corrsin–Obukhov law for passive scalars gives an accurate description of the horizontal stratification of the atmosphere including its intermittency. We also argued that by extending this further to anisotropic space–time, the overall result could be used as the basis for a turbulence/wave model in which spatially and temporally localized turbulent fluxes provide the sources for unlocalized velocity and density fluctuations. This model was based on an energy flux dominating the horizontal and a buoyancy force variance flux dominating the vertical (both of which are quadratic invariants and hence should be conserved scale by scale). In contrast to the main quasi-linear gravity wave models – which require a weakly nonlinear state in order to justify the use of linear dispersion relations – this model assumes that the atmosphere is highly heterogeneous and turbulent.

---

* Correspondence to: S. Lovejoy, Department of Physics, McGill University, 3600 University St, Montreal, QC, Canada, H3A 2T8.
E-mail: lovejoy@physics.mcgill.ca

In Lilley *et al.* (2004) and in part II, we used airborne lidar data to test a key quantitative difference between the gravity wave and turbulence wave models; the stratification of space (x, y, z) is characterized by $D_s = 1 + 1 + 1/3 = 7/3$ in the former, whereas by $D_s = 1 + 1 + 5/9 = 23/9$ in the latter. Since we found empirically from vertical cross-sections of lidar backscatter ratio that $D_s = 2.55 \pm 0.02$, the evidence was firmly in favour of the turbulence wave model (with a small (± 0.02) but systematic decrease for more intense structures, larger q). However, the model predicted the full space–time statistical scaling behaviour; it uses classical Kolmogorov-type arguments to argue that for the full space–time domain (x, y, z, t), $D_{\mathrm{st}} = D_{\mathrm{s}} + H_t'$. For more full validation, we must therefore turn to the time domain to estimate H_t'. In this paper, we therefore seek to extend the vertical (x, z) analyses to space–time (z, t) analyses.

2. Temporal scaling in the atmosphere

2.1. Pure temporal development, horizontal or vertical dominance?

Following the classical Kolmogorov approach, we may obtain the scaling law for horizontal and temporal velocity fluctuations using dimensional analysis based on the fact that the nonlinear terms of the Navier–Stokes equations conserve energy fluxes. The idea is that there is a quasi-steady energy flux input from large scales balanced (on average only) by kinetic energy dissipation at small scales. Since the kinetic energy flux (per unit of mass) across an eddy (structure) with shear Δv is $\varepsilon = \Delta v^2/\tau$, we need only estimate the characteristic time for the transfer, τ. For fluctuations in the horizontal, the only time-scale available is $\tau = \Delta x/\Delta v \Rightarrow \Delta v = \varepsilon^{1/3}\Delta x^{H_{\mathrm{h}}}$ with $H_{\mathrm{h}} = 1/3$ which is the familiar Kolmogorov result. (In Fourier space, the corresponding isotropic energy spectrum – ignoring intermittency – is $E(k) \approx k^{-\beta_{\mathrm{h}}}$; $\beta_{\mathrm{h}} = 1 + 2H_{\mathrm{h}} = 5/3$.)

In time, there are two classical approaches to estimating the fluctuations. The first is to consider a Lagrangian framework (following the mean flow); dimensional analysis yields $H_\tau = 1/2$ (Inoue, 1951; Landau and Lifshitz, 1959); this gives a spectral exponent $\beta_\tau = 1 + 2H_\tau = 2$. In cases where there is a very low mean velocity, the Eulerian (fixed frame) is equivalent, so that in this case of 'pure' temporal development we expect $H_\tau = 1/2$. At the other extreme, if the turbulence is blown past with mean velocity U so quickly that it is practically 'frozen' (i.e. it satisfies the conditions of Taylor's (1938) 'frozen turbulence' hypothesis), then we can use the horizontal law but with $\Delta x = u\Delta t$ so that $\Delta v = \varepsilon^{1/3}U^{1/3}\Delta t^{H_{\mathrm{h}}}$ so that $H_\tau = H_{\mathrm{h}}1/3$ (hence $\beta_\tau = 1 + 2H_\tau = 5/3$).

Basing his work on the experimental results of Comte-Bellot and Corrsin (1971) and Shlien and Corrsin (1974), Tennekes (1975) argued that, even in a flow with zero mean velocity, the largest eddies would 'sweep' the small eddies past a fixed point and that this effect would dominate the temporal Eulerian statistics. In part I, we discussed this quantitatively with the help of space–time scale functions, and showed that indeed, for times below the eddy turnover time of the largest eddy, this is likely to be true. However, this analysis ignored intermittency and assumed that the Kolmogorov scaling held in the horizontal all the way to planetary scales; it is therefore important to return to this question with the help of empirical evidence (section 2.2). Also as pointed out in part I, in the 23/9-D model there is the additional source for a roughly $\beta_\tau \approx 2$ spectrum – a scaling vertical velocity.

The prediction that the temporal spectral exponent β_τ would typically be either 5/3 or 2 is in accord with many of the observations surveyed in part II and, as mentioned in part I, the main gravity wave theories assume $\beta_\tau = 2$ (the saturated cascade theory) or β_τ in the range 5/3 to 2 (the exact value is not so important) in the Diffusive Filtering Theory. The experimental literature (Table I) gives a review and highlights two possible temporal exponents $\beta_\tau = 5/3$ and $\beta_\tau = 2$. The value of the scaling exponent is not clear from the experimental results; it seems that it is indeed variable although mostly in the range 5/3 to 2. In most papers the experimentalists did not consider two different behaviours, e.g. Beatty *et al.* (1992) claimed $\beta_\tau = 1.85 \pm 0.23$ averaged over 21 days; this value is also between 5/3 and 2. It seems plausible that averaging was made over periods with different values of β_τ. On the other hand, Gardner and Voelz's (1987) claim of the difference between winter and summer results (the former is compatible with Taylor's hypothesis and the latter is compatible with vertical wind domination; see section 2.2 for discussion) is also plausible because the vertical wind might be much stronger during summer due to increased convection.

2.2. Using meteorological analyses to identify different temporal scaling regimes

In the 23/9-D model, the time/horizontal structure is basically unchanged in comparison with isotropic Kolmogorov turbulence; what is new is the vertical structure which gives rise to a third term for the temporal development. To see this, recall the anisotropic space–time generalization of the classical Kolmogorov law given in part I:

$$|\Delta v(\Delta \mathbf{R})| = \varepsilon^{1/3}_{[\![\Delta \mathbf{R}]\!]}[\![\Delta \mathbf{R}]\!]^{1/3}, \quad (1)$$

where $\Delta \mathbf{R} = (\Delta x, \Delta y, \Delta z, \Delta t)$ and $[\![\Delta \mathbf{R}]\!]$ is a space–time scale function and Δv is the velocity difference between two points separated by $\Delta_{\mathbf{R}}$. If we include advection, we saw that the simplest 'canonical scale function' (part I, Equation (27)) is:

$$\begin{aligned}[\![\Delta \mathbf{R}]\!] &= [\![(\Delta \mathbf{r}, \Delta t)]\!]_{\mathrm{can}} \\ &= l_s\left[\left(\frac{\Delta x - u\Delta t}{l_s}\right)^2 + \left(\frac{\Delta y - v\Delta t}{l_s}\right)^2\right. \\ &\quad \left. + \left(\frac{\Delta z - w\Delta t}{l_s}\right)^{2/H_z} + \left(\frac{\Delta t}{\tau_s}\right)^{2/H_t}\right]^{1/2}, \quad (2)\end{aligned}$$

Table I. Review of empirical evidence.

Author and year	Experimental technique	Quantity measured	Observations made by author	Frequency range (Hz)	Spectral exponent β measured
Hwang (1970)[a]	Anemometers of the three-cup generator and counter types	Wind speed	Atmospheric turbulence follows $-5/3$ power law.	$3 \times 10^{-7} - 1 \times 10^{-4}$ $1 \times 10^{-5} - 6 \times 10^{-2}$	Reference $\beta_\tau = 5/3$ is shown.
Balsley and Carter (1982)[b]	MST radar	Horizontal wind speed at altitudes 8 and 86 km	Resulting curve corresponds very well to $\omega^{-5/3}$ slope out to the high-frequency limit.	$3 \times 10^{-3} - 1 \times 10^{-7}$ $6 \times 10^{-3} - 4 \times 10^{-7}$	Reference $\beta_\tau = 5/3$ is shown.
Larsen *et al.* (1982)[c]	MST radar	Horizontal wind speed at several altitudes from 6 to 15 km	Spectra follow $-5/3$ power law in period range 2–50 hours. Refer to Taylor's transformation and $-5/3$ power law for horizontal wavenumber.	$3 \times 10^{-7} - 3 \times 10^{-4}$	β_τ from 1.24 to 2 are obtained, depending on wind component and altitude.
Scheffler and Liu (1985)[d]	MST radar	Horizontal wind speed	Acoustic gravity wave theory proposed that quantitatively relates the MST radar observed wind fluctuation spectrum.	$2 \times 10^{-5} - 2 \times 10^{-2}$	$\beta_\tau = 2$ fits data very well.
Balsley and Garello (1985)[e]	MST radar	Horizontal wind speed	No theoretical explanation offered.	$3 \times 10^{-7} - 1 \times 10^{-3}$	$\beta_\tau = 2$ fits stratospheric (13.4 km) data in frequency range $10^{-4} - 10^{-6}$ Hz and tropospheric (9.1 km) data in range $\sim 8 \times 10^{-4} - 10^{-6}$ Hz.
Meek *et al.* (1985)[f]	MST radar	Horizontal wind speed	The slope of the best-fit line is ~ 1.5	$4 \times 10^{-7} - 3 \times 10^{-4}$ $5 \times 10^{-5} - 3 \times 10^{-3}$	Reference $\beta_\tau = 1.5$ is shown. Exponent 5/3 fits data.
Gardner and Voelz (1987)[g]	Lidar	Na density	$-5/3$ power law is predicted.	$2 \times 10^{-5} - 7 \times 10^{-4}$	Observed β_τ: 2.18 summer, 1.73 winter.
Kwon *et al.* (1990)[h]	Radar, ground-based and airborne lidar	Wind speed, Na density	No theoretical explanation offered.	$3 \times 10^{-5} - 1 \times 10^{-2}$	Whole Na layer $\beta_\tau = 1.52$; top side of the layer $\beta_\tau = 1.12$, bottom side $\beta_\tau = 1.77$
Fritts *et al.* (1990)[i]	MU Radar	Wind speed	No theoretical explanation offered.	$1 \times 10^{-5} - 2 \times 10^{-3}$	Reference $\beta_\tau = 5/3$ and 2 are shown.

Table I. (*Continued*).

Author and year	Experimental technique	Quantity measured	Observations made by author	Frequency range (Hz)	Spectral exponent β measured
Beatty *et al.* (1992).[j]	Rayleigh/Na lidar	Passive scalar concentration	No theoretical explanation offered.	$9 \times 10^{-5} - 3 \times 10^{-3}$ (range for linear regression)	Single day $\beta_\tau = 1.7$; average β_τ over 21 nights = 1.85 ± 0.23
Sica and Russell (1999)[k]	Rayleigh/Na lidar	Passive scalar concentration	Average exponent of 2 claimed.	$5 \times 10^{-5} - 2 \times 10^{-2}$	β_τ from 1.2 to 2.7

[a] The data used to construct the wide frequency-range power density spectrum were taken by an MRI anemometer from 1500 LST on 14 March to 1200 LST on 1 May 1967, and by the AN/GMQ-12 anemometer from 1105 LST on 10 April to 1600 LST on 18 April 1967.

[b] Time ranges for wind fluctuations: at 8 km from 6 minutes to 83 days, at 86 km from 3 minutes to ~30 days.

[c] Zonal and meridional wind measurements made with the Poker Flat MST radar over a 40-day period were used to calculate the frequency power spectra at heights between 5.99 and 14.69 km. The finest temporal resolution was 1 hour. Regression was made for frequencies in the range 0.015–0.45 h^{-1}. In some cases this range included an obviously noisy range.

[d] The time range was from 1 to ~750 minutes. No linear regression was made by the authors.

[e] Horizontal wind values were formed into 4096-point datasets comprising 34 day sequences of 12-minute averaged data points. No linear regression was made by the authors.

[f] 1 to 720 hour time series and 33 series from 5 min to 6 h were used.

[g] Observed periods were from 25 to 800 min.

[h] Time series from 100 s to ~8 h were used. Temporal regressions were made over time-scales from 30 to 360 min. Top-side layer spectrum looks noisy, the bottom-side layer spectrum fits −5/3 power law quite well.

[i] Spectra at higher altitudes look noisy, but fit $\beta_\tau = 5/3$. Lower altitude spectra fit $\beta_\tau = 2$ well.

[j] Temporal resolution was 2 min for Na data and 5 min for Rayleigh data. Linear regression fits were performed over the frequency range $\sim(3\ \mathrm{h})^{-1}$ to $(5\ \mathrm{min})^{-1}$. The authors did not separate cases close to exponents of 5/3 and 2, which is why the confidence interval is rather wide (1.62–2.06).

[k] Strong deviations from $\beta_\tau = 5/3$ and $\beta_\tau = 2$ were observed in the cases when the regression includes obvious high- and/or low-frequency artefacts.

where $\Delta\mathbf{r} = (\Delta x, \Delta y, \Delta z)$, the wind velocity is (u, v, w) and the sphero-scale (l_s) is the scale at which horizontal and vertical fluctuations are of equal magnitude, and the sphero-time, τ_s, is the eddy turnover time (eddy lifetime) at the sphero-scale. Below we consider a limited spatial domain with horizontal wind components u and v as arbitrary constants given by the large scale but with vertical component w as a random field. This leads to a new 'effective' advected generator $G_{\mathrm{eff,adv}}$ (see part I) and 'effective' scale function; first, however, we consider the theoretical generator with non-random constant w.

For temporal fluctuations at a spatial point (i.e. $\Delta\mathbf{r} = (0, 0, 0)$ and taking our x-axis parallel to the horizontal wind, so that $v = 0$) we obtain the following scale function:

$$[\![\Delta t]\!] = [\![(0, 0, 0, \Delta t)]\!] = l_s \left\{ \left(\frac{u\Delta t}{l_s}\right)^2 + \left(\frac{w\Delta t}{l_s}\right)^{2/H_z} + \left(\frac{\Delta t}{\tau_s}\right)^{2/H_t} \right\}^{1/2}. \tag{3}$$

We now see that the horizontal advection term $(u\Delta t/l_s)^2$ dominates the pure temporal development term $(\Delta t/\tau_s)^{2/H_t}$ for all $\Delta t < \Delta t_{xt}$, where:

$$\Delta t_{xt} = \frac{u^2}{\varepsilon}, \tag{4}$$

where we have used $H_t = 2/3$ and $\varepsilon = l_s^2 \tau_s^{-3}$. The Tennekes 'sweeping' result can now be obtained by taking $\Delta v \approx u$ for the largest eddy, so that for this eddy (scale L; planetary-scale structures), the turnover time $\tau_{\mathrm{e},L}$ is u^2/ε, so that $\Delta t_{tx} \approx \tau_{\mathrm{e},L}$. Thus, according to this analysis, the critical time estimated above for the domination of pure temporal development over the horizontal wind term is the eddy turnover time of the largest eddies, which in part I we argued was the synoptic maximum, i.e. about 2 weeks (see below for direct empirical estimates).

This result does not involve the new vertical wind term; it is therefore classical. However, when we consider the 23/9-D model with scale function Equation (3), we can see that we must also consider the new vertical advection term $(w\Delta t/l_s)^{2/H_z}$. Since $H_z < H_t < 1$, we can see that for constant w (the "naïve" view) this term will be dominant for large enough Δt. There are thus two new pairs of terms to consider; in obvious notation, we have the following new critical times:

$$\Delta t_{tz} = \tau_s \left(\frac{v_s}{w}\right)^6, \tag{5a}$$

$$\Delta t_{xz} = \left(\frac{l_s}{w}\right)\left(\frac{u}{w}\right)^{5/4}, \tag{5b}$$

In part I we have discussed the consequences of a scaling vertical velocity; this has the effect of giving vertical advection domination at the scale $\Delta t'_{xz}$ (Equation (75), part I). Where $w = w_l$, an intermittent scaling vertical velocity, and H_t the effective temporal exponent, we obtain:

$$\Delta t'_{xz} = \frac{u^2}{\varepsilon}\left(\frac{v_s}{w}\right)^3\left(\frac{l_s}{l}\right)^{3(H'_t - H_z)}, \tag{5c}$$

(using $H_z = 5/9$, $H_t = 2/3$ and $v_s = l_s/\tau_s$). We now see that, while the horizontal advection will dominate at small enough Δt because $H_z < H_t < 1$, there will only be a pure temporal development zone if $\Delta t_{xt} < \Delta t_{xz}$ (or $\Delta t_{xt} < \Delta t_{xz}$ for variable, non constant w). Since the time-scales Δt_{xt}, Δt_{xz}, Δt_{tz}, Δt_{xz} are highly variable and depend on the resolution of the data, we now attempt to evaluate them empirically.

In order to determine Δt_{xt}, Δt_{xz}, Δt_{tz}, $\Delta t'_{xz}$ we used meteorological analyses from a component of the operational Canadian Meteorological Centre Global Environmental Multiscale (GEM) model, the North America regional GEM model. The original analysis is on a variable-step grid with a 15 km central core resolution. We used the low-resolution (60 km at 60) fields on a 135 × 95 polar-stereographic grid covering North America (and adjacent waters) over a region which includes the North Pole. Vertical coverage of 3-D fields is provided by 28 isobaric levels. Detailed information about the model is available at Environment Canada's web site (http://weatheroffice.ec.gc.ca/grib/Low-resolution_GRIB_e.html). Although the grid is not exactly rectangular, it is close enough so that we assume that four nearest pixels to some fixed pixel lie on two orthogonal lines going through it.

To start with, we performed a spectral analysis of the lowest level of the analysis for which vertical wind data was available: 850 hPa ~ 1450 m above sea level. We first checked that the noon and midnight GMT analyses were statistically very similar and close to $k^{-5/3}$ for the horizontal wind (so that the theory could plausibly be applied). We confirmed that there is quite good horizontal scaling with an exponent not far from the Kolmogorov value 5/3. (The slope is a little steeper for horizontal sections at the higher altitudes where the analyses are less reliable.)

Since the transition times depend on l_s, τ_s and the latter depend on the highly intermittent fluxes, ε, ϕ, we first show the probability distributions of the latter (Figure 1). As a technical point, we calculated the fluxes using $\varepsilon = \Delta v(\Delta x)^3/\Delta x$, $\phi = \Delta v(\Delta z)^5/\Delta z^3$ for horizontal wind gradients in the horizontal and vertical respectively. We see that the distribution has a very long tail; in fact the general result from cascade theory is that the 'dressed' cascaded quantities (i.e. those which result from a cascade carried from large to infinitely small scales and then averaged up to an intermediate 'observation' scale) should be asymptotically algebraic, i.e.

$$\Pr(\varepsilon_\lambda > s) \approx s^{-q_D}; \quad s >> 1$$

(Mandelbrot, 1974; Schertzer and Lovejoy, 1987). The figure confirms this behaviour and we obtain an exponent

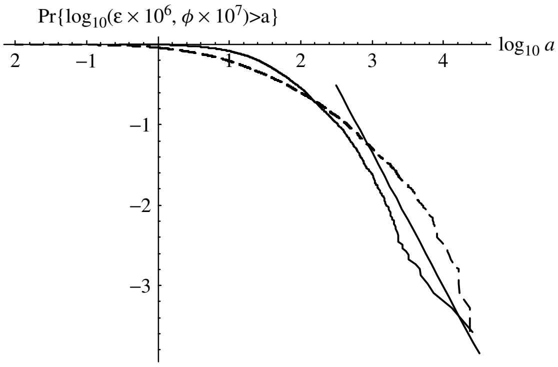

Figure 1. Probability distributions of the energy flux $\varepsilon \times 10^6$ (m^2 s^{-3} solid) and the buoyancy force variance flux $\phi \times 10^7$ (m^2 s^{-5} dashed), averaged over 4 vertical layers (950–750 hPa; 540–2460 m) and 300 km (5 pixels) in the horizontal. Eight realizations are used. A reference slope showing the theoretical behaviour $\Pr(\varepsilon_\lambda > s) \approx s^{-q_D}$ with $q_D = 1.66$ is shown.

close to the value $q_D = 1.66$, the empirical value found for ε in the vertical in Schertzer and Lovejoy (1985) (see also the similar aircraft results in Lovejoy and Schertzer, 2007). That this behaviour is very extreme is evident from the fact that since $q_D < 2$, the variance diverges whereas the mean barely converges (since q_D is only a little greater than one).

In Figure 2 we calculate the corresponding l_s, τ_s, $v_s = l_s/\tau_s$ values using 'bare' formulae which are good approximations (appendix A of part I):

$$l_s = \varepsilon_\lambda^{5/4}\phi_\lambda^{-3/4}, \quad \tau_s = \varepsilon_\lambda^{1/2}\phi_\lambda^{-1/2}, \quad v_s = l_s/\tau_s. \tag{6}$$

Since $q_{D\varepsilon} \approx 1.66$, if the l_s, τ_s, v_s distributions are dominated by large ε (rather than small ϕ), we expect $q_{Dls} = 1.66/(5/4) \approx 1.33$, $q_{D\tau s} = 1.66/(1/2) \approx 3.33$, $q_{vls} = 1.66/(3/4) \approx 2.22$. From Figure 2, we see that these predictions are fairly well respected; this shows that the data are internally consistent, and also consistent with radiosonde data in Schertzer and Lovejoy (1985). The fact that the $q_D > 1$ shows that the means are well

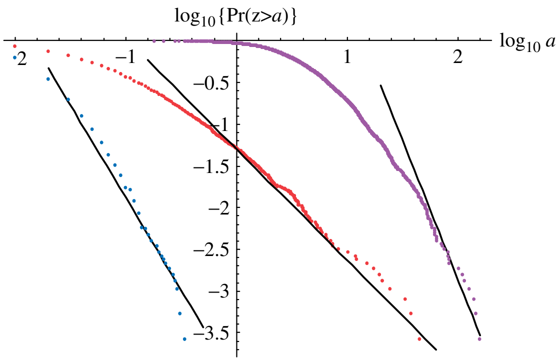

Figure 2. Cumulative probability distributions of v_s (m/s; left), l_s (m; centre) and τ_s (s; right), calculated at horizontal resolution of ~300 km (5 pixels). Energy flux calculated at 850 hPa level; buoyancy flux is averaged over 4 layers between 950 hPa (~540 m) and 750 hPa (~2460 m). Reference slopes of −20/9 (v_s), −4/3 (l_s), and −10/3 (τ_s) and are shown. This figure is available in colour online at www.interscience.wiley.com/qj

defined. In the case of l_s, we see that the values are generally <1 m, although there are about 5% which are >1 m (the mean is 30 cm), with the extreme of nearly 10 m. Similarly, the sphero-time is typically <10 s (the mean is 7.2 s), but ranges up to 100 s while the sphero-speed is typically of the order of cm s^{-1} with the largest value 20 cm s^{-1} (the mean is 2.2 cm s^{-1}).

Finally, we turn to the time-scale estimates; Figure 3 shows plots of the cumulated probability distributions. As we can see, as predicted by Tennekes' argument, the probability is low ($<45\%$) that the critical Δt_{xt} for the transition from horizontal to temporal dominance to be less than the eddy turnover time at the largest model scale ($\sim$6000 km; estimated here as 9.5×10^5 s), the probability that the transition occurs at times less than 3 hours is $<2\%$. The Δt_{xt} time can be regarded as a local estimate of the planetary eddy turnover time; it is therefore interesting to compare it to the probability distribution of eddy turnover times for eddies 300 km in size: $\tau_{\mathrm{e},l} = \varepsilon^{-1/3} l^{2/3}$ (curve 4). The fact that this curve is much steeper than the others indicates that the eddy turnover time is quite well defined (around 3 hours in this case; this is the effective time-scale of our 300 km degraded pixels). However, even if the pure temporal development term dominates the horizontal advection term, we cannot conclude that it will be the overall dominant term; we must show that it also dominates the vertical advection term. Certainly, by considering the transition time Δt_{tz}, we see that Δt_{tz} is typically much smaller than Δt_{xt} so that, even when it dominates the horizontal advection term, it does not dominate the vertical term.

We now turn our attention to the Δt_{xz} transition time, which gives us information about when to expect vertical wind dominance over the horizontal advection term. Here, we give two curves; one for the 'naïve formula' Equation (5b) (curve 2) and the other $\Delta t'_{xz}$ using the 'effective' generator discussed in part I (Equation 5c and especially appendix B; curve 3). Recall that, unlike the horizontal wind which has a well-defined mean over a large region, the vertical velocity fluctuates around zero, converging to zero in a (presumably) scaling way as the space–time scale of the averaging increases. If, as postulated in part I, the mean vertical wind over time-scale Δt scales as $w \approx \Delta t^{H_w}$ with $H_w < 0$, then the vertical advection term $(w\Delta t/l_s)^{1/H_z}$ gives an effective temporal scaling exponent $H'_t > H_z$; below we argue on the basis of lidar data that empirically $H'_t \approx H_t$. Curve 3 in Figure 3 shows this distribution of the corresponding time-scale $\Delta t'_{xz}$ when this effective $(w\Delta t/l_s)^{1/H_z}$ term dominates. We see that it has the effect of making the vertical term larger so that the probability of an effective vertical term dominating the horizontal advection term becomes appreciable ($\approx$5%), even for periods as short as 100 s. Recall that this estimate is for 300 km horizontal scales, i.e. an effectively 3-hour temporal resolution (see the eddy turnover time above); this is roughly the scale of the lidar datasets studied below. It is thus at least plausible that, for somewhat shorter resolution data, the probability will be a little higher and we will be able to observe the vertical dominance regime at scales of 10–100 s. This is particularly true since we expect the vertical dominance to be more likely in lower, generally more unstable, atmospheric layers. It should be mentioned that the meteorological data we analyzed is for the autumn season, not summer which again should be more convectively unstable, increasing the likelihood of vertical wind dominance; the lidar data was taken in June. Finally, we should mention that we have analyzed another eight (z, t) lidar datasets, all of which apparently gave horizontal wind dominance, so, including the six analyzed here, we have three out of 14 showing vertical wind dominance.

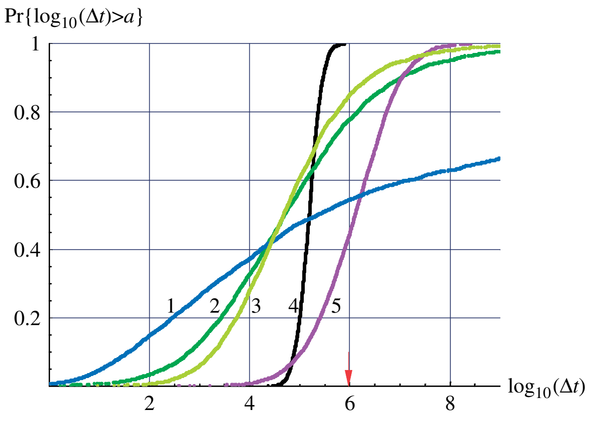

Figure 3. Cumulative probability distributions of transition times. 1 is Δt_{tz}, calculated from a 'naïve' point of view without taking into account temporal scaling of the vertical velocity; 2 is Δt_{xz}; 3 is Δt_{xz}, calculated from the 'naïve' point of view; 4 is the eddy turnover time; 5 is Δt_{xt}. All are calculated at the resolution degraded by a factor of 5 ($\sim$300 km). The arrow shows the eddy turnover time calculated at the largest scale 9.5×10^5 s. This figure is available in colour online at www.interscience.wiley.com/qj

2.3. The space–time scaling for passive scalars

We have seen in parts I, II and in the introduction how the classical Kolmogorov law can be extended to anisotropic space–time scaling behaviour taking into account the buoyancy variance fluxes in the vertical. The key part of the model – including the wave/turbulence model in part I – involves the replacement of the usual Euclidean distance by a scale function. In part II, we saw how this could be used to obtain an anisotropic extension of the classical Corrsin–Obukhov law for passive scalar diffusion in the stratified (x, y, z) space. First, we ignored the y coordinate (equivalently, orienting our system so that the x-axis is parallel to the horizontal component of the wind). Extending this to averages over a space–time region scale l (taken for simplicity to be a reduction by factor λ of the largest space–time region, the outer scale of the cascade), we have for the space–time averaged density structure function (averaged over scale l):

$$\langle |\Delta\rho(\Delta\mathbf{r}, \Delta t)|^q \rangle_l = \varphi_\lambda^{q/3} l^{K_\varphi(q/3)} [\![(\Delta\mathbf{r}, \Delta t)]\!]^{\xi(q)};$$

$$\varphi = \chi^{3/2}\varepsilon^{-1/2};$$

$$\xi(q) = qH_\mathrm{h} - K_\varphi(q/3);$$

$$[\![(\Delta\mathbf{r},\Delta t)]\!] = \Theta(\widehat{\Omega}')[\![(\Delta\mathbf{r},\Delta t)]\!]_{\mathrm{can}};$$

$$[\![(\Delta\mathbf{r},\Delta t)]\!]_{\mathrm{can}} = \left[\left(\frac{\Delta x - u\Delta t}{l_s}\right)^{2} + \left(\frac{\Delta z}{l_s}\right)^{2/H_z} + \left(\frac{\Delta t}{\tau_s'}\right)^{2/H_t'}\right], \qquad (7)$$

where $H_\mathrm{h} = 1/3$ and $\widehat{\Omega}'$ is a unit vector (in the non-linearly transformed 'primed' space, see part I and below) so that $\Theta(\widehat{\Omega}')$ represents the shape of unit ball, $[\![(\Delta\mathbf{r},\Delta t)]\!]_{\mathrm{can}}$ is the canonical scale function (see section 2.2 and part I, Equation (27)), χ is the passive scalar variance flux, ϵ the energy flux, K_φ is the moment scaling exponent characterizing the intermittency, and ξ_φ is the corresponding structure function exponent. Note that this expression was derived by using the multiplicative nature of the cascade from the large external scale L down to the region of data analysis (scale l, an anisotropic reduction by factor $L/l = \lambda$). This allows us to factor out the low-frequency flux φ_λ; the effect of the averaging over the remaining high frequencies in Equation (7) is approximated by ensemble averages. If we ensemble average both sides of Equation (7), we obtain an exact expression; however since we apply our analysis to individual realizations, we need Equation (7) (see part I appendix A for more discussion).

In Equation (7) we consider the horizontal component u to be constant; there is no explicit vertical component w since the statistics of w are accounted for via H_t' and τ_s'; see part I. The canonical scale function corresponds to the 'effective' space–time generator (part I, Equation (31); see also appendix B of part I for definitions of τ_s' and H_t' and appendix A of part I for the statistical definition of l_s, taking into account intermittency, including the effect of ensemble averaging the spatially averaged Equation (6)). Just as l_s will depend on q, so will the shape of the unit ball $\Theta(\widehat{\Omega}')$.

3. Analysis in orthogonal directions: vertical, time

3.1. Vertically pointing lidar data

We have seen that, due to the effects of advection, the temporal scaling is expected to be somewhat more complex than the pure spatial scaling discussed in part II. In particular, we anticipate that, on the basis of the meteorological analyses of part II, over a period of several hours – in cases with particularly strong vertical motion and particularly weak horizontal motion – we may occasionally observe anomalous temporal scaling corresponding to dominance of the vertical term in the scale function.

In this section, we use ground-based, upward-pointing lidar data from the PACIFIC 2001 experimental campaign, as well as data from the MSC CARE facility in order to obtain (z, t) sections of lidar backscatter, our surrogate for passive scalar concentration. We first analyse the exponents in order to attempt to check whether the data are horizontally or vertically dominated; we then estimate the 'trivial scaling' $\Theta(\widehat{\Omega}')$ function using the new Anisotropic Scaling Analysis Technique (ASAT), applying it also to the vertical section data of part II.

The ground-based laser was operated at the fundamental wavelength of 1064 nm, suited for the detection of particles with diameter of the order of 1 m and had a pulse repetition rate of 10 Hz (Strawbridge and Snyder, 2004). The measured backscatter ratio B was averaged over various time intervals (Table II); the result was a 2-D vertical–time planar section. All the detectors used log amplifiers – important due to the wide dynamical range of the backscatter.

Table II presents the main characteristics of the experimental datasets. Figures 4–7 show some original lidar pictures.

3.2. Analysis in the vertical

Before turning to a more complete analysis of the data, we can already check Equation (7) above by considering the 1-D spectra only in time or only in the vertical; in 1-D this is estimated from the (possibly) ensemble-averaged squared modulus of the (numerical) Fourier transform of the series. Here we use the term 'spectrum' in order to follow traditional term usage referring to the second-order statistics Fourier analysis. For the spectrum, we use the standard notation E which evokes 'energy' even though, strictly speaking, E generally does not have units of energy per mass. In Figure 8 we can clearly see the Bolgiano–Obukhov (BO) scaling in the vertical. Some deviations from the theoretically predicted slope are due to problems with lidar attenuation corrections (see especially the second spectrum from the top in Figure 8). This means that values of the backscatter ratio are too smooth over the highest factor of 8 or so in scale. In this connection we should mention that the airborne lidar is much less affected by attenuation. This is because most of the backscatter is near the ground. In order to eliminate this systematic effect, we remove the mean vertical profile from each cross-section. Another problem arises due to the inadequate dynamical range of the digitizer so that – to within one digital count – successive raw values are nominally the same, i.e. spuriously smoothed (Gagnon *et al.* (2006) provides a quantitative analysis of this effect). In this case (Egbert0602) we avoided the problem by degrading the vertical resolution by a factor of 8 before proceeding to the refined 2-D analyses discussed below. In terms of 1-D spectra, this is roughly equivalent to the highest frequencies with steep spectral fall-off. As far as we can tell, the cirrus and aerosol scalings are the same and both are compatible with the anisotropic extension of the Corrsin–Obukhov law. We can see that the BO value $= 11/5$ works well over a wide range of scale (up to two orders of magnitude).

3.3. Analysis in time

To determine the temporal behaviour for vertical–time datasets, we made standard 1-D spectral analyses in time.

Table II. Main parameters of experimental datasets.

Dataset name	Type of data	Object type	Resolution[a]	Dimensions[b]
Langley0807[c]	Vertical-time	aerosol	2.997 × 1.0s	300 × 4990
Langley0808[c]	Vertical-time	aerosol	2.997 × 1.0s	300 × 5036
Egbert0530[d]	Vertical-time	cirrus cloud	3.746 × 0.5s	904 × 11468
Egbert0602[d]	Vertical-time	cirrus cloud	3.746 × 30.0s	1536 × 828
Egbert0603[d]	Vertical-time	aerosol	3.746 × 30.0s	486 × 648
Egbert0616[d]	Vertical-time	cirrus cloud	3.746 × 30.0s	800 × 752
Pacific0815t6[e]	Vertical-horizontal	aerosol	2.997 × 100.0m	372 × 952
Pacific0815t8[e]	Vertical-horizontal	aerosol	2.997 × 100.0m	844 × 776
Pacific0815t22[e]	Vertical-horizontal	aerosol	2.997 × 100.0m	956 × 932
Pacific0814t5[e]	Vertical-horizontal	aerosol	2.997 × 100.0m	384 × 750
Pacific0814t7[e]	Vertical-horizontal	aerosol	2.997 × 100.0m	386 × 846
Pacific0814t9[e]	Vertical-horizontal	aerosol	2.997 × 100.0m	372 × 846

[a] The first number is vertical resolution (m), and the second is time or horizontal resolution. The horizontal resolution of vertical–horizontal section datasets is estimated with an aircraft speed of 100 m s^{-1}.

[b] (Vertical × time) or (vertical × horizontal).

[c] acquired with ground-based lidar during PACIFIC 2001 in Langley, British Columbia on 7, 8 August.

[d] Egbert0530, Egbert0602, Egbert0603 and Egbert0616 are from a CARE 2003 ground-based lidar experiment, acquired in Egbert, Ontario on 30 May, 02, 03 and 16 June respectively.

[e] PACIFIC 2001 airborne lidar platform experiments acquired in the Lower Fraser Valley, BC on 14, 15 August (see part II).

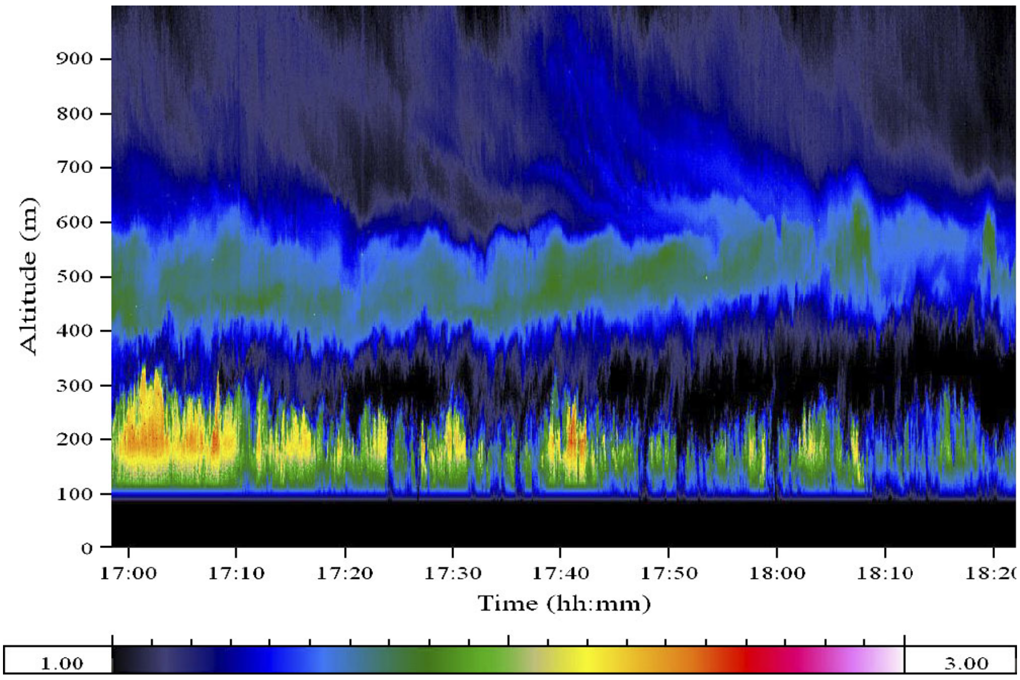

Figure 4. Langley0808 data taken on 8 August 2001, for a case of horizontal wind dominance. The scale is linear: darker is for smaller backscatter (aerosol density surrogate), lighter for larger backscatter. If we assume that the slopes of structures in the figure are purely due to the vertical wind, then 45 slopes correspond to $w \sim 0.40$ m s^{-1}. There are no bad pixels in the image. There is no saturated signal and there is high sensitivity to low signal return. This figure is available in colour online at www.interscience.wiley.com/qj

The results are represented by Figure 9; we see that there are three cases with $\beta_\tau \approx 2$ (Egbert0602, Egbert0603 and Langley0807), and three other cases showing $\beta_\tau \approx 5/3$. Ignoring intermittency, these spectra correspond to $H_\tau = (\beta_\tau - 1)/2 = 1/2,\ 1/3$. Since in the vertical we found $\beta_v \approx 11/5$, we have $H_v = (\beta_v - 1)/2 = 3/5$, and thus $H_t \approx H_\tau/H_v \approx 2/3, 5/9$ for $H_\tau = 1/2, 1/3$ respectively. As we have shown, although it is very unlikely to observe pure temporal development from time-scales below around 10^4–10^5 s (Figure 3), it is quite possible to occasionally observe vertical wind dominance over horizontal wind. Figure 3 shows that, for a somewhat higher part of the atmosphere at a less convective time of year, this could occur for a few percent of the time even at 10^2 s. Since, for these three datasets, we observe reasonable spectral ω^{-2} scaling without any clear scale

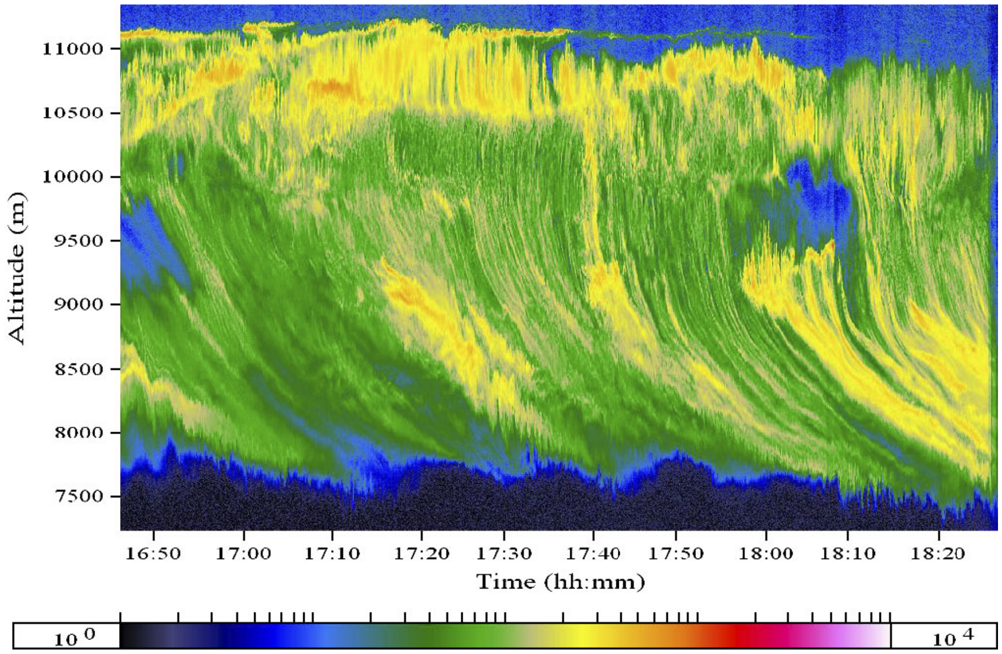

Figure 5. Egbert0530 data taken on 30 May 2003, for a case of horizontal wind dominance. The scale is logarithmic: darker is for smaller backscatter (cirrus density surrogate), lighter is for larger backscatter. Structures at 45 correspond to $w \sim 0.75$ m s^{-1}. There is no saturated signal and there is high sensitivity to low signal return. This figure is available in colour online at www.interscience.wiley.com/qj

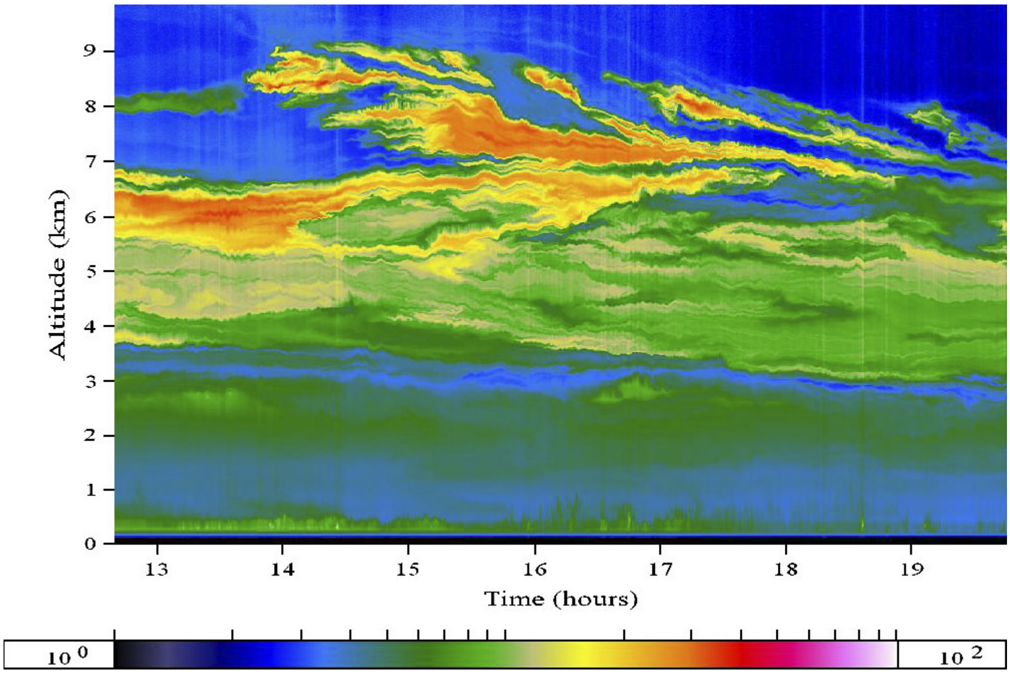

Figure 6. Egbert0602 data taken on 2 June 2003, for a case of vertical wind dominance. The scale is logarithmic: darker is for smaller backscatter (cirrus density surrogate), lighter is for larger backscatter. Structures at 45 correspond to $w \sim 0.50$ m s^{-1}. There is no saturated signal and there is high sensitivity to low signal return. This figure is available in colour online at www.interscience.wiley.com/qj

breaks, we consider that these three cases are examples of vertical wind-dominated development.

4. Arbitrary directions in space–time

4.1. The ASAT

In sections 3.2, 3.3, we analysed the data in orthogonal directions (vertical, time). This is only a partial analysis; it does not allow us to test the theory at intermediate angles in (z, t) space, nor estimate the function characterizing the 'trivial anisotropy' $\Theta(\widehat{\Omega}')$. We now describe the new ASAT for doing this. In this section, we will illustrate the technique on $q = 1$ (first-order) structure functions and 2-D data (primarily the (z, t) data discussed above), but we also revisit the (x, z) data used in part II. Since our spectral analyses have shown that none of our six datasets have clear scale breaks in time, we conclude

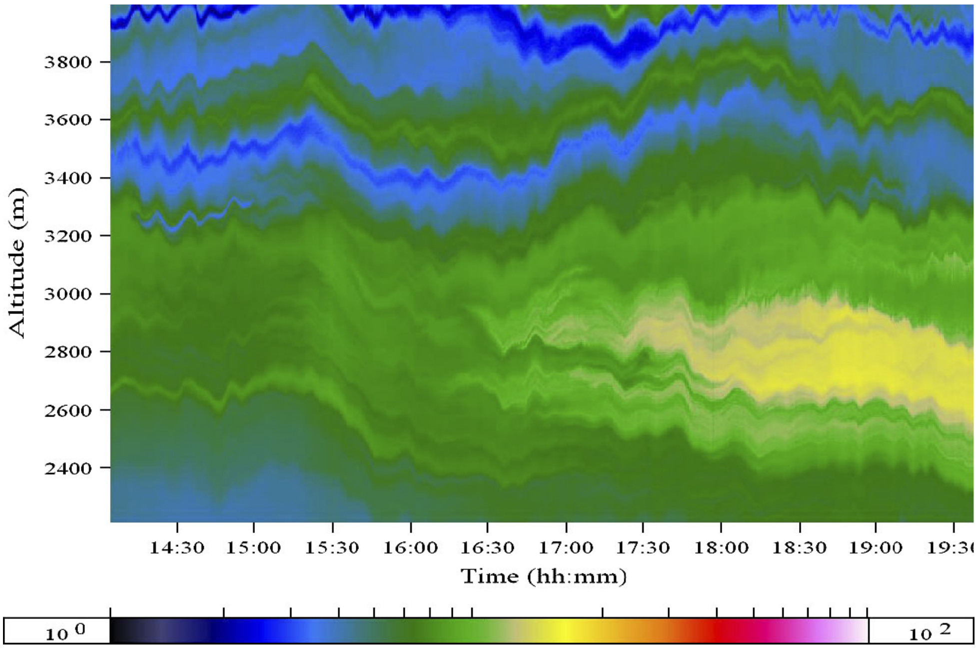

Figure 7. Egbert0603 data taken on 3 June 2003, for a case of vertical wind dominance. The scale is logarithmic: darker is for smaller backscatter (aerosol density surrogate), lighter is for larger backscatter. Structures at 45 correspond to $w \sim 0.15$ m s^{-1}. There is no saturated signal and there is high sensitivity to low signal return. This figure is available in colour online at www.interscience.wiley.com/qj

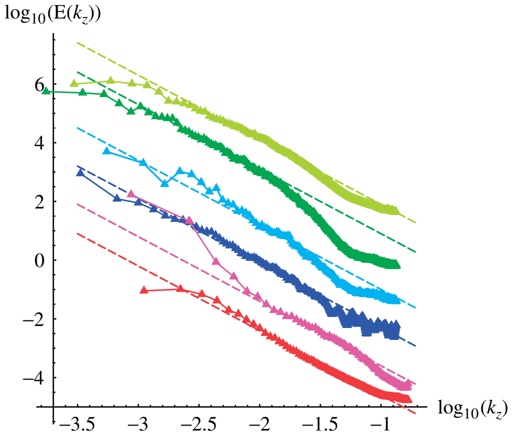

Figure 8. 1-D space (vertical) spectra as function of vertical wavenumber k (m^{-1}) for vertical–time datasets (offset in the vertical for clarity). Top to bottom: Egbert0530 (cirrus cloud), Egbert0602 (cirrus), Egbert0603 (aerosol), Egbert0616 (aerosol), Langley0807 (aerosol), Langley0808 (aerosol). Dashed lines are reference theoretical slopes of −11/5. This figure is available in colour online at www.interscience.wiley.com/qj

that they are each dominated by a single temporal scaling regime, corresponding to domination by either horizontal or vertical advection. In these cases of pure temporal scaling, from Equation (7), we see that for $q = 1$, we write either horizontal or vertical domination as

$$\begin{aligned}\Delta\rho(\Delta z, \Delta t) &= (|\Delta\rho(0, 0, \Delta z, \Delta t)|)_{(l_z,\tau)}\\ &= \varphi_\lambda^{1/3} l_s^{1/3} \Theta^{1/3}(\theta_\mathrm{p}'')\\ &\quad\times\left[\left(\frac{\Delta z}{l_s}\right)^{2/H_z} + \left(\frac{\Delta t}{\tau_s^*}\right)^{2/H_t^*}\right]^{1/6}, \quad (8)\end{aligned}$$

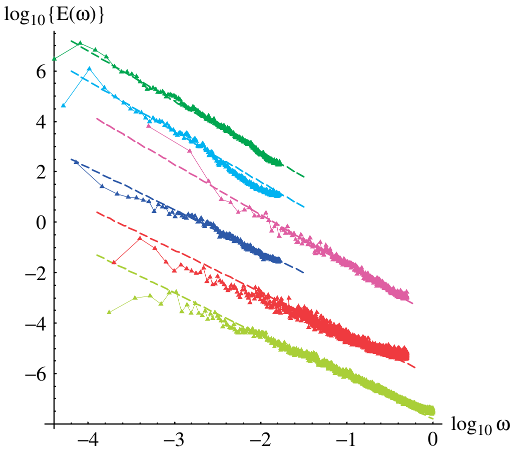

Figure 9. 1-D time spectra as functions of frequency ω (s^{-1}) for vertical–time datasets (offset in the vertical for clarity). Bottom to top: Egbert0530 (cirrus cloud), Langley0808 (aerosol), Egbert0616 (aerosol), Langley0807 (aerosol), Egbert0603 (aerosol), and Egbert0602 (cirrus). Dashed lines are reference theoretical slopes of −2 (top three) and −5/3 (bottom three). This figure is available in colour online at www.interscience.wiley.com/qj

where we have taken $H_\mathrm{h} = 1/3$ and introduced a product of conservative fluxes $\varphi = \chi^{3/2}\varepsilon^{-1/2}$ and neglected the intermittency corrections for this low-order moment, i.e. taken K_φ (1/3) $\approx$0, and have introduced Θ which is function only of the polar angle θ_p'' in the nonlinearly transformed space (see part I, and Equations (9) and (11) below). As indicated, $\Delta\rho(\Delta z, \Delta t)$ is the abbreviated notation for the spatial mean (over the space–time region (l_z, τ) of the absolute density fluctuation in the (z, t) plane. We take $H_t^* = 1$, $\tau_s^* = l_s/u$ for horizontal wind domination and $H_t^* = H_t' \approx 2/3$, $\tau_s^* = \tau_s'$ for vertical wind domination.

We shall introduce another simplifying step for the (z, t) analyses. It is convenient to introduce another form of scale function in the (z, t) domain:

$$\begin{aligned}
[\![(\Delta z, \Delta t)]\!]_{\mathbf{G}^*} &= \Theta^*(\theta'_{\mathrm{p}}) l_s \left[\left(\frac{\Delta t}{\tau_s^*}\right)^2 + \left(\frac{\Delta z}{l_s}\right)^{2/h} \right]^{1/2} \\
&= \Theta^{H_t^*}(\theta''_{\mathrm{p}}) l_s \\
&\quad \times \left[\left(\frac{\Delta t}{\tau_s^*}\right)^{2/H_t^*} + \left(\frac{\Delta z}{l_s}\right)^{2/H_z} \right]^{H_t^*/2}; \\
\theta'_{\mathrm{p}} &= \arctan\left(\frac{\mathrm{sign}(\Delta z)|\Delta z/l_s|^{1/h}}{\Delta t/\tau_s^*} \right); \\
\theta''_{\mathrm{p}} &= \arctan\left(\frac{\mathrm{sign}(\Delta z)|\Delta z/l_s|^{1/H_z}}{\mathrm{sign}(\Delta t)|\Delta t/\tau_s^*|^{1/H_t^*}} \right); \\
\mathbf{G}^* &= \mathbf{G}/H_t^*; \quad h = H_z/H_t^*. \qquad (9)
\end{aligned}$$

This new scale function satisfies the basic scaling equation (see part I) with generator $\mathbf{G}^* = \mathbf{G}/H_t^*$; $\Theta^*(\theta'_{\mathrm{p}})$ determines the trivial anisotropy for this new scale function. The advantage of this new scale function is that under the simple transformation which is only nonlinear with respect to one of the coordinates:

$$\Delta t' = l_s \Delta t/\tau_s^*, \quad \Delta z' = l_s(\Delta z/l_s)^{1/h}\mathrm{sign}(\Delta z), \quad (10)$$

$$R' = (\Delta z'^2 + \Delta t'^2)^{1/2}, \quad \theta'_{\mathrm{p}} = \arctan\left(\frac{\Delta z'}{\Delta t'}\right), \quad (11)$$

it is reduced to a scale function which is symmetric with respect to isotropic ($\mathbf{G} = 1 =$ identity matrix) scale transformations. (The coordinate transformation (10) is already of this form for vertical (x, z) sections). Obviously, the transformation could have been chosen with Δz rather than Δt being the linear transformation. However the datasets at our disposal spanned a much wider range of scales in the time direction, so this would have led to a large mismatch in available scales in the Δz compared to Δt directions.

The (x, z) plane fluctuations can be written in the analogous way:

$$\begin{aligned}
\Delta\rho(\Delta x, \Delta z) &= (|\Delta\rho(\Delta x, 0, \Delta z, 0)|)_{(l_x, l_z)} \\
&= \varphi_\lambda^{1/3} l_s^{1/3} \Theta^{1/3}(\theta'_{\mathrm{p}}) \\
&\quad \times \left[\left(\frac{\Delta x}{l_s}\right)^2 + \left(\frac{\Delta z}{l_s}\right)^{2/H_z} \right]^{1/6}, \quad (12)
\end{aligned}$$

with notation analogous to that used in Equation (8) and

$$\Delta x' = \Delta t; \quad \Delta z' = l_s(\Delta z/l_s)^{1/H_z}\mathrm{sign}(\Delta z). \quad (13)$$

In this nonlinear ('primed') space, we have the following polar coordinates:

$$R' = (\Delta x'^2 + \Delta z'^2)^{1/2}; \quad \theta'_{\mathrm{p}} = \arctan\left(\frac{\Delta z'}{\Delta x'}\right), \quad (14)$$

so in all cases, we may write:

$$\Delta\rho(R', \theta') \sim \Theta^{1/3}(\theta'_{\mathrm{p}}) R'^{1/3}, \quad (15)$$

where $\Theta(\theta'_{\mathrm{p}})$ represents the shape of all the balls in the $(\Delta x', \Delta z')$ space. The virtue of this nonlinear transformation is that, in $(\Delta x', \Delta z')$ space, the scaling is symmetric under isotropic scale transformations, i.e. with $\mathbf{G} =$ the identity so that more traditional isotropic analysis methods can be used (see part I). $\Theta(\theta'_{\mathrm{p}})$ thus determines the remaining 'trivial' anisotropy in the primed space; hence it also determines the unit ball in $(\Delta x', \Delta z')$ space. Equations (12)–(15) are the basis of the ASAT. It allows us to simultaneously verify the anisotropic scaling hypothesis (15) in arbitrary non-orthogonal directions while determining the function $\Theta(\theta'_{\mathrm{p}})$ in the space $(\Delta x', \Delta z')$. In the next sections we discuss how to use structure functions and spectra to estimate Θ, and in section 4.3 we discuss the interpretation of the result.

When performing numerical analysis, we use spatial and temporal resolutions as convenient natural units of spatial displacement and time lag, respectively (so that distances and times can be given in dimensionless spatial and temporal 'pixels'; the shape function $\Theta(\theta'_{\mathrm{p}})$ will depend on this choice). This means that the l_s will be expressed in units of spatial pixels, and τ_s in units of time steps.

4.2. The ASAT in real space: anisotropic structure functions

To empirically verify Equation (15), we consider the $q = 1$ (first-order) 2-D structure function dependence on primed radial polar coordinate R' for fixed value of angle θ'_{p} in the $(\Delta z', \Delta t')$ and $(\Delta x', \Delta z')$ spaces. We have already given the equation for the first-order spatially averaged structure function (Equations (8) and (12)); in the nonlinearly transformed (isotropic) space, in polar coordinates, we may write (for both (x, z) and (z, t) cross-sections):

$$S_1(R', \theta'_{\mathrm{p}}) = |\Delta\rho|. \quad (16)$$

In section 4.3 we consider the effects of intermittency using higher-order structure functions; these will be small for this low-order ($q = 1$) moment. Testing this on the data, we obtain Figures 10(a), 11(a), 12(a), and 13(a). As one can see by the parallel lines for various values of θ, the theory works well over a wide range of scales for both cirrus clouds and aerosols, for both horizontal and vertical advection-dominant cases of temporal development. The difference between the 1-D structure functions in different directions means that the unit ball is not a circle (sphere). To clearly see this 'trivial' anisotropy $\Theta(\theta'_{\mathrm{p}})$, we remove the theoretically expected R' dependence by calculating the 'compensated' 2-D structure function, $S_{\mathrm{c},1} = R'^{-1/3} S_1(R', \theta'_{\mathrm{p}})_{\mathrm{p}}$. If the theory and hence the transformation defining R', θ' is correct, then $S_{\mathrm{c},1} = \Theta^{1/3}(\theta'_{\mathrm{p}})$ i.e. it is just a function of θ'_{p}; it determines the shape of the unit ball. Figures 10(b),

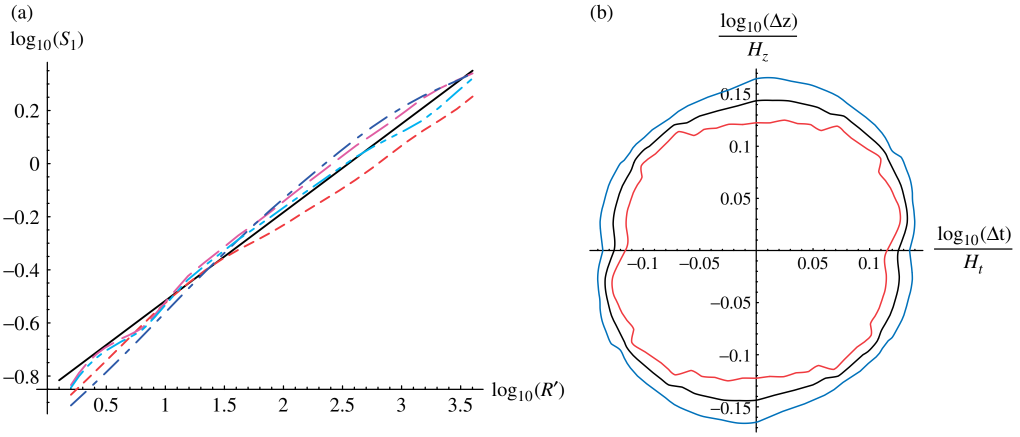

Figure 10. (a) 2-D structure function S_1 as a function of R' for four directions: $\theta'_{\mathrm{p}} = 0$ (short dashes, corresponding to $R' = \Delta t'$), $\pi/4$ (long dashes), $\pi/2$ (dash-dot, corresponding to $R' = \Delta z'$), and $3\pi/4$ (dash-dot-dot) in the nonlinearly transformed ($\Delta z'$, $\Delta t'$) space for Egbert0603. The solid line is the theoretical slope of 1/3. (b). Polar plot of compensated structure function $S_{\mathrm{c},1} = R'^{-1/3}S_1(\log_{10}(R'), \theta'_{\mathrm{p}})$ averaged over $0.2 < \log_{10}(R') < 3.4$ for Egbert0603 (centre line), with angle representing the direction of ($\Delta x'$, $\Delta z'$) and distance from the origin representing the size of $S_{1,\mathrm{c}}$. Quantities $\log_{10}(\Delta t)/H_t$ and $\log_{10}(\Delta z)/H_z$ show distance from the centre of the plot in time and vertical directions but they are not Cartesian coordinates. Outer/inner lines indicate plus/minus one standard deviation. This figure is available in colour online at www.interscience.wiley.com/qj

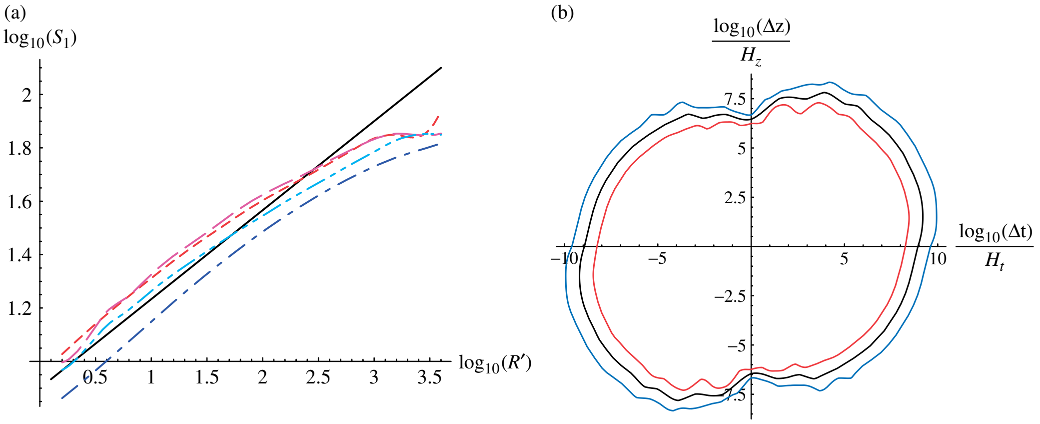

Figure 11. As Figure 10, but for Egbert0530. In (b), the averaging is over $0.2 < \log_{10}(R') < 2.6$. This figure is available in colour online at www.interscience.wiley.com/qj

11(b), 12(b), and 13(b) were determined from tables of $S_{\mathrm{c},1} = R'^{-1/3}S_1$ values as functions of $\log_{10}(R')$ and θ'_{p} with increments of $\log_{10}(R') = 0.2$. Along rays of fixed angle θ'_{p}, the relative error (the ratio of the standard deviation to mean $S_{\mathrm{c},1}$ and to the mean of $S_{\mathrm{c},1}$) does not exceed 10% over wide ranges of scale ($R'_{\mathrm{max}}/R'_{\mathrm{min}} > 10^3$ in many instances); often this variation does not exceed 5% (Figure 14(b)). The ranges chosen for averaging are indicated in the captions for the figures. Thus, ASAT analysis applied to first-order ($q = 1$) 2-D structure functions allows us to verify the theory to within about 10% over more than 3 orders of magnitude of space–time or space–space scales, and this at various angles in (z', t') space. Note that, from their definitions, the structure functions are symmetric with respect to inversion about the origin.

While the near-constancy of the compensated structure functions as functions of angle gives strong support to the correctness of the coordinate transformation and passive scalar theory (the exponent 1/3 in the first of Equations (7)), one can also use the technique to test the alternatives, the $D_s = 7/3$ gravity waves, and the $D_s = 3$ isotropic turbulence. This can be easily done by using the corresponding nonlinear coordinate transformations and visually checking for the constancy of the resulting Θ functions.

Figures 14(a), (b) and (c) show a comparison of contour plots of $\log[S_1(\log(R'/R_i), \theta'_{\mathrm{p}})]$ with nonlinear transformation (10) (or (11)) corresponding to different models: isotropic turbulence, the 29/9-D model and quasi-linear gravity waves. If the contours of $\log\{S_1(R', \theta'_{\mathrm{p}})\}$ are invariant under an isotropic scale change (i.e. they have the same shapes), then the corresponding contours of $\log[S_1\{\log(R'/R_i), \theta'_{\mathrm{p}}\}]$ will not have the same shapes but they will be rather equally spaced in all directions (R_i is a non-dimensionalizing inner scale; below R_i, the signal is dominated by instrumental noise). The advantage of using a $(\log(R'/R_i), \theta'_{\mathrm{p}})$ space representation is that we can visually represent a much wider range of scales on the same

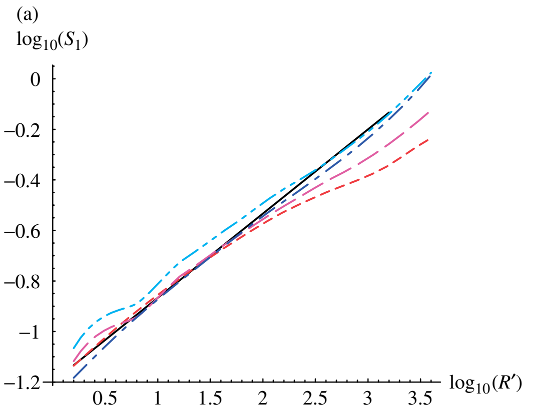

Figure 12. As Figure 10, but for Langley0807. In (b), the averaging is over $0.2 < \log_{10}(R') < 2.4$. This figure is available in colour online at www.interscience.wiley.com/qj

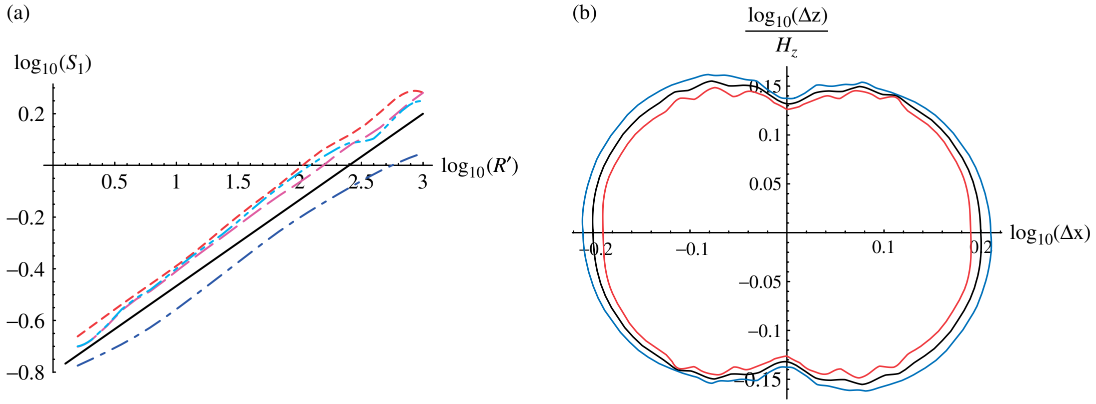

Figure 13. As Figure 10, but for Pacific0815t6. In (b), the averaging is over $0.2 < \log_{10}(R') < 2.8$. This figure is available in colour online at www.interscience.wiley.com/qj

picture. The analysis is done using the alternative scale function Equation (9). For the left column corresponding to $h = H_z/H_t^* = 1$ (i.e. no transformation of coordinates), we can see that as we move from contour to contour, the spacing between the contours is different in the horizontal and vertical directions. In the centre column (using the theoretical transformation from the 29/9 model, i.e. $H_t = 2/3$), we can see that the contours are spaced pretty much the same distance apart (i.e. equally spaced in all directions as expected). Finally in the right-hand column, the gravity wave value of $h = H_z/H_t^*$ is used in the transformation, again leading to contours which are not equally spaced – this time they are closer in the vertical than in the horizontal. Note that all the contours are spaced at equal factors of S_1 of 1.12 (for the 23/9 model, i.e. with $H_\mathrm{h} = 1/3$, this corresponds to a factor of 1.41 in scale); the total range of scales is roughly 100.

4.3. Multifractal analysis in space–time

4.3.1. Discussion

Until now, we have applied ASAT to confirm the anisotropic space–time scaling extensions of the Corrsin–Obukhov law; we did not use it to empirically estimate the theoretical exponents. In Radkevich *et al.* (2007), we show one way of doing this. Here, we return to the method of part II (orthogonal directions), but consider the anisotropy of the moments of all orders (i.e. including the effects of intermittency). All the results discussed above were obtained for first- or second-order statistics, S_1, E, respectively.

Consider first the advection-free cascade starting at a large outer space–time scale (L_x, L_z, T) with data taken at the region (l_x, l_z, τ) which is (anisotropically) reduced by factor λ. As discussed in appendix A of part I, the qth-order structure functions spatially averaged over the space–time region (l_x, l_z, τ) are given by:

$$\begin{aligned}
&\langle|\Delta\rho(\Delta x,0,0,0)|^q\rangle_{(l_x,l_z,\tau)}\\
&\quad= \varphi_\lambda^{q/3}\left(\frac{l_x}{\Delta x}\right)^{K_\varphi(q/3)}\Delta x^{q/3} = \varphi_\lambda^{q/3} l_x^{K_\varphi(q/3)}\Delta x^{\xi_h(q)};\\
&\langle|\Delta\rho(0,0,\Delta z,0)|^q\rangle_{(l_x,l_z,\tau)}\\
&\quad= \kappa_\lambda^{q/5}\left(\frac{l_z}{\Delta z}\right)^{K_\kappa(q/5)}\Delta z^{3q/5} = \kappa_\lambda^{q/5} l_z^{K_\kappa(q/5)}\Delta z^{\xi_v(q)};\\
&\langle|\Delta\rho(0,0,0,\Delta t)|^q\rangle_{(l_x,l_z,\tau)}\\
&\quad= \chi_\lambda^{q/2}\left(\frac{\tau}{\Delta t}\right)^{K_\chi(q/2)}\Delta t^{q/2} = \chi_\lambda^{q/2}\tau^{K_\chi(q/2)}\Delta t^{\xi_\tau(q)},
\end{aligned} \tag{17}$$

(a) Egbert 0530, wind domination

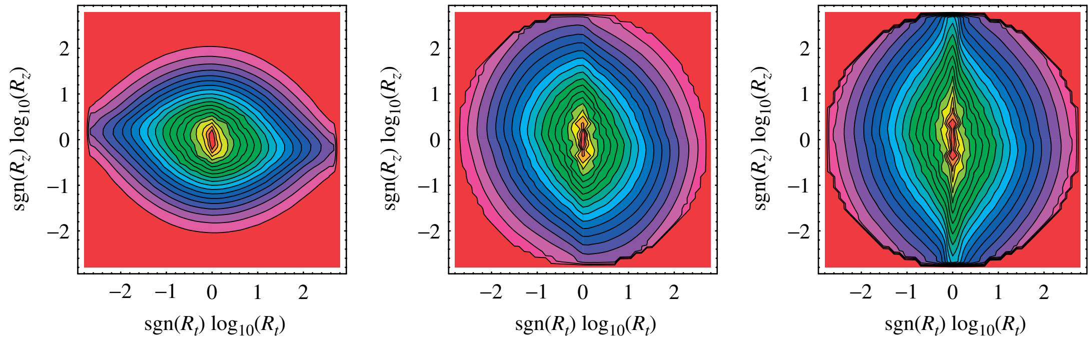

(b) Egbert 0603, vertical wind domination

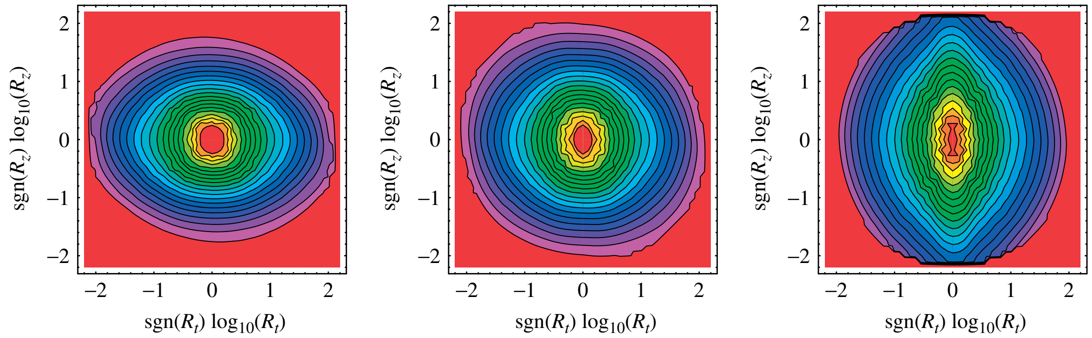

(c) Pacific 2001 0815t6, vertical–horizontal cross-section

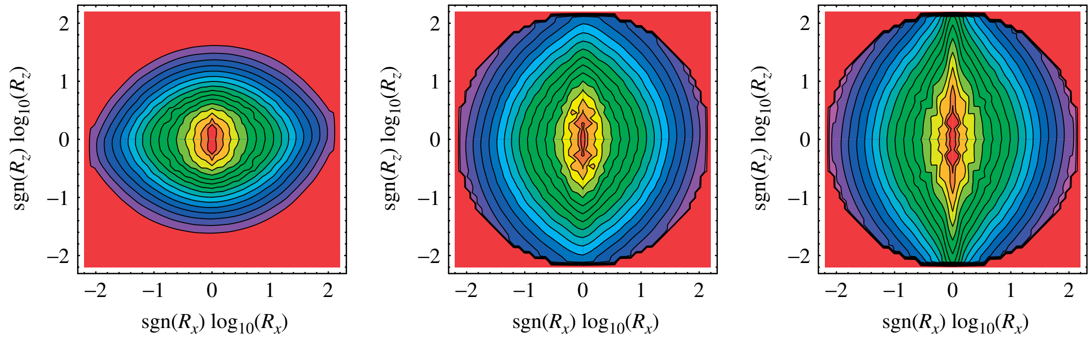

Figure 14. Contour plots of S_1 with three different nonlinear transformations: left, no transformation (isotropy); centre, the 23/9-D model discussed in the text; right, the gravity wave model. The three cases (a), (b), (c) correspond to (z, t) horizontal wind domination, (z, t) vertical wind domination and vertical cross-sections (x, z), respectively. In the left column $h = 1$; in the centre column $h =$ (a) $H_z/H_t' = 5/9$, (b) $H_z/H_t' = 5/6$, (c) $H_z = 5/9$ (see Equation (10) for cases (a) and (b) and (13) for (c)); in the right column $h =$ (a) 1/3, (b) 1/2, (c) 1/3. We use the notation $R_x = \Delta x'$, $R_z = \Delta z'$, $R_t = \Delta t'$. Note that, although $\mathrm{sgn}(R_t)\log_{10}(R_t)$, $\mathrm{sgn}(R_x)\log_{10}(R_x)$ and $\mathrm{sgn}(R_z)\log_{10}(R_z)$ show the distance from the centre of the plot in the corresponding direction, they are not Cartesian coordinates of the plot. This figure is available in colour online at www.interscience.wiley.com/qj

where we have introduced the product of conserved fluxes $\kappa = \chi^{5/2}\varepsilon^{-5/2}\phi$ and ξ_h, ξ_v, ξ_τ are the structure function exponents of the corresponding fluxes:

$$\begin{aligned}\xi_h(q) &= q/3 - K_\varphi(q/3),\\ \xi_v(q) &= 3q/5 - K_\kappa(q/5),\\ \xi_\tau(q) &= q/2 - K_\chi(q/2),\end{aligned}\tag{18}$$

where $K_\varphi(q)$, $K_\kappa(q)$, $K_\chi(q)$ are the moment scaling exponents of the fluxes φ, κ, χ respectively.

We now consider the effect of advection; this will only affect the temporal exponents. We have already argued that the pure temporal scaling behaviour assumed in Equations (17), (18) is likely to be academic due to advection effects. The two behaviours that we found empirically were identified with either horizontal advection domination, or vertical advection domination. These are obtained by taking $\llbracket(0, 0, 0, \Delta t)\rrbracket = u\Delta t$ and $\llbracket(0, 0, 0, \Delta t)\rrbracket = l_s(\Delta t/\tau_s')^{1/H_t'}$ respectively; they lead to:

$$\begin{aligned}&(|\Delta\rho(0, 0, 0, \Delta t|^q)_{(l_x,l_z,\tau)}\\ &\quad= \varphi_\lambda^{q/3}\left(\frac{\tau}{\Delta t}\right)^{K_\varphi(q/3)}(u\Delta t)^{q/3}\\ &\quad= \varphi_\lambda^{q/3}\tau^{K_\varphi(q/3)}(u\Delta t)^{\xi_h(q)},\end{aligned}\tag{19a}$$

$$(|\Delta\rho(0, 0, 0, \Delta t|^q)_{(l_x,l_z,\tau)}$$

$$= \varphi_\lambda^{q/3}\left(\frac{\tau}{\Delta t}\right)^{K_\varphi(q/3)/H_t'}\left(l_s\left(\frac{\Delta t}{\tau_s'}\right)^{1/H_t'}\right)^{q/3}$$

$$= \varphi_\lambda^{q/3}\tau^{K_\varphi(q/3)/H_t'}l_s{}^{q/3}\tau_s'^{-q/(3/H_t')}\Delta t^{\xi_h(q)/H_t'}. \quad (19b)$$

The top equation (19a) is for horizontal wind domination and u is assumed constant across the data region; we ignore possible intermittency effects in u. These are not expected to be significant since for the horizontal velocity (unlike the vertical velocity) $H_\mathrm{h} > 0$, so that the scale dependence is in gradients Δu, not in the mean. In comparison, the lower equation (19b) assumes vertical wind domination with the effective generator resulting from the presumed scale dependence of the mean vertical velocity (see appendix B in part I for more details). According to this interpretation, the τ_s' is determined by the mean vertical velocity over the region via the equation $\tau_s' = \tau_s(v_s/w_l)(l/l_s)^{H_z - H_t'}$, where l is the effective scale of the data region (the region of averaging), so that w_l is the overall mean vertical velocity due to the large-scale variability (at scales larger than the averaging region). These two different scalings yield:

$$\xi_\tau(q) = \begin{cases} \xi_\mathrm{h}(q) & u \text{ dominant} \\ \xi_\mathrm{h}(q)/H_t' & w \text{ dominant} \end{cases} \quad (20)$$

The anisotropy exponents are now given by the ratios:

$$H_z = \frac{\xi_\mathrm{h}(q)}{\xi_\mathrm{v}(q)} = H_{z,1} + \Delta H_z; \quad H_{z,1} = \frac{5}{9},$$
$$H_t = \frac{\xi_\mathrm{h}(q)}{\xi_\tau(q)} = H_{t,1} + \Delta H_t; \quad H_{t,1} \approx 0.66,$$
$$H_{zt} = \frac{\xi_\tau(q)}{\xi_\mathrm{v}(q)} = H_{zt,1} + \Delta H_{zt}; \quad H_{zt,1} = \frac{H_{z,1}}{H_{t,1}}. \quad (21)$$

We have broken up the anisotropy exponents into basic non-intermittent components ($H_{z,1}$, $H_{t,1}$, $H_{zt,1}$) and small intermittent corrections ($\Delta H_{z,1}$, $\Delta H_{t,1}$, $\Delta H_{zt,1}$). The value of $H_{t,1}$ is based on the 'effective' scale function (see part I) Since there is a one-to-one relation between structures, singularities and statistical moments, this small q dependence will tell us about the variation of the space–time anisotropy with the intensity of the structure. Note that although the basic non-intermittent value $H_{z,1} = 5/9$ is the same as for the velocity field, this presumably is not true of the intermittency corrections. In addition, the temporal value $H_{t,1}$ has two values depending on whether there is horizontal or vertical dominance. We have indicated the rough estimates based on the spectra in Equation (19); below we estimate them more precisely.

4.3.2. *Mean anisotropy exponents*

Before calculating the ratio of structure function exponents in order to estimate the anisotropy exponents, we display Figures 15(a) and (b) which give an indication of the quality of the estimates. First, we consider the consistency with which they estimate the vertical exponents (Figure 15(a); these should be the same irrespective of whether there is horizontal or vertical wind dominance), and the intercomparison with the airborne results of part II (Figure 15(b)). In Figure 15(a) we note that, starting with low q, all the values of ξ_v agree very well, however they eventually disagree at large enough q. This is a consequence of the fact that, after a certain critical q, a single large singularity can dominate the statistics. Since one of the structure functions (for Egbert0807) falls off quickly after $q \approx 1.5$, we put it aside in order to calculate the ensemble mean up to moments of order $q = 3$; this is shown in Figure 15(b) where we also show the ξ_v for ensemble mean of the the airborne lidar data in part II. Recall that the attenuation is more severe for the ground-based lidar used in part III; it appears that the attenuation has been adequately dealt with since the two values of $\xi_\mathrm{v}(q)$ agree to within one standard deviation up to $q = 3$.

We now consider the overall mean anisotropy, first on the parametric plot of ξ_v versus ξ_τ in Figure 16

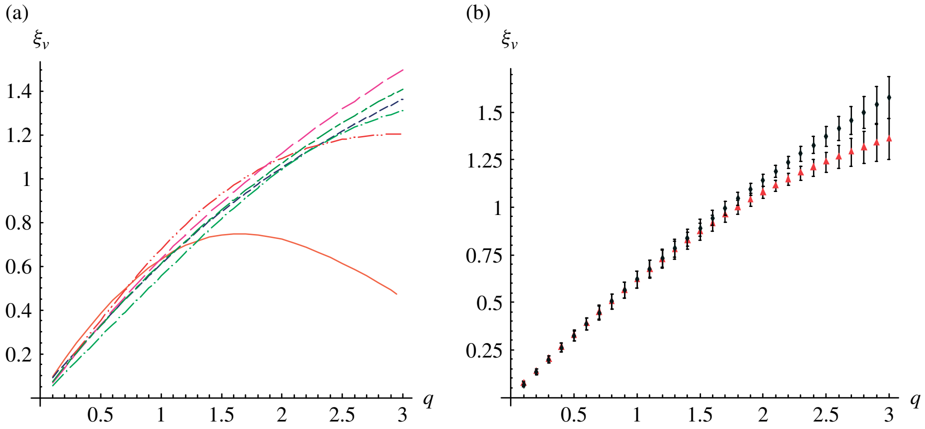

Figure 15. Structure function scaling exponent ξ_v as a function of the order of statistics q: (a) different vertical–time cross-sections: Langley0807 (solid), Langley0808 (short dash), Egbert0530 (dash dot), Egbert0616 (dash dot dot), Egbert0602 (long dash), Egbert0603 (long dash short dash). (b) average value over several realizations with standard deviation as error bars; black diamonds are vertical–horizontal cross-sections (see part II), and triangles are vertical–time cross-sections (average over 5 cases from (a) without Langley 0807). This figure is available in colour online at www.interscience.wiley.com/qj

(analogous to Figure 9 in part II). Although – as in Figure 15 – we see deviations from linear behaviour occur at high values of q due to poor statistics, the basic low-q behaviour is quite linear although it clearly breaks into two families, with slopes close to the theoretical value ($H_{tz,1} = 5/9$, horizontal wind domination) and a slope close to the theory for vertical wind domination with $H'_t = 2/3$, i.e. $H_{tz,1} = (5/9)/(2/3) = 5/6$.

Before considering the small deviations from linearity, we will consider the average behaviour by averaging over all values of q between 0 and 3 at intervals of 0.1. For the three cases with horizontal wind domination, we find an average $H_{tz,1} = \xi_\tau/\xi_\mathrm{v} = 0.54 \pm 0.02$ (theory predicts 5/9); for the cases of vertical wind domination $H_{tz,1} = \xi_\tau/\xi_\mathrm{v} = 0.81 \pm 0.04$ (theory predicts $(5/9)/0.66 = 0.83$).

In order to find the temporal exponent $H'_{t,1} = H_{tz,1}/H_{z,1}$, we must make an assumption for $H_{z,1}$. Assuming the theoretical value $H_{z,1} = 5/9$, we obtain $H'_{t,1} \approx 0.68 \pm 0.03$. Alternatively, assuming that H_z is the mean structure function exponent ratio for the wind domination case $\xi_\tau/\xi_\mathrm{v} = 0.54 \pm 0.02$ (very close to theoretical prediction of 5/9), we obtain $H_{t,1} = (0.54 \pm 0.02)/(0.81 \pm 0.04) = 0.67 \pm 0.06$. Thus, using either the theoretical value of the stratification exponent of H_z or the experimental one, we obtain compatible estimates of H'_t. Finally, we obtain the effective elliptical dimension of space–time atmospheric motions which is the trace of the generator $\mathbf{G}_\mathrm{st}$:

$$D_\mathrm{st,eff,advec} = \mathrm{Tr}(\mathbf{G}_\mathrm{st}) = 2 + H_{z,1} + H'_{t,1}. \tag{22}$$

The corresponding experimental values based on theoretical and empirical $H_{z,1}$ are $D_\mathrm{st,eff,advec} \approx 3.24 \pm 0.03$ and $D_\mathrm{st,eff,advec} \approx 3.21 \pm 0.06$, respectively.

4.3.3. *The small q-dependent corrections*

We now consider the small deviations from linearity in Figure 16. Figures 17(a) and (b) show dependencies of intermittency corrections ΔH_z, ΔH_t on the order of statistics (see part I, appendices A and B for theoretical considerations). These corrections are calculated as the ratios ξ_t/ξ_z with subtraction of the corresponding stratification exponent ($H_{z,1}$ or $H_{t,1}$) for cases of horizontal wind domination (ΔH_z) and vertical wind domination (ΔH_t). Figure 17(a) compares intermittency corrections ΔH_z for different types of data cross-sections ((x, z) and (z, t)). For the horizontal wind dominance, the agreement is to within about 0.01 with the results for vertical sections (part II). One can see that estimated intermittency corrections for two experimental campaigns are in satisfactory agreement. Figure 17(b) shows theoretical corrections calculated with formula (part I, appendix B):

$$\Delta H'_t = \frac{H_{z,1}}{1 + \dfrac{H_{z,1}}{\xi_\mathrm{h}(q)}\xi_w\left(\dfrac{\xi_\mathrm{h}(q)}{H_{z,1}^2}\right)} - H_{t,1}, \tag{23}$$

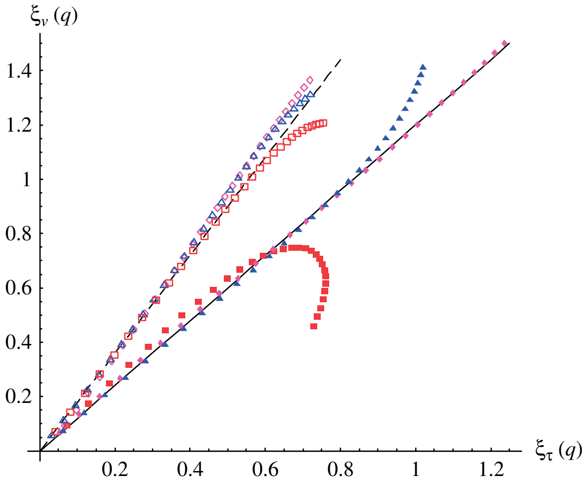

Figure 16. Parametric dependence of $\xi_\tau(q)$ versus $\xi_v(q)$ ($q = 0.1, 0.2, \ldots, 3$) for three cases of horizontal wind domination and three cases of vertical wind domination. The slopes of reference theoretical lines are $H_t/H_z = 9/5$ (dashed) and $H_t/H_z = 6/5$ (solid). Data from: Langley0807 (solid boxes), Egbert0603 (solid triangles), Egbert0602 (solid diamonds), Egbert0616 (open boxes), Egbert0530 (open triangles) and Langley0808 (open diamonds). This figure is available in colour online at www.interscience.wiley.com/qj

where we used $H_{z,1} = 5/9$ and $H_{t,1} = 2/3$ and we assumed that vertical wind exponent ξ_w is a universal multifractal with $\alpha_w = 1.8$, C_{1w}, $H_w = -0.13$ as indicated (α_w and C_{1w} are chosen to be close to those of the horizontal wind; cf. Lovejoy *et al.*, 2007). We have not attempted an optimum fit; to a first approximation, the result is very insensitive to α_w – the value of H_w adjusts the curve vertically, and the value of C_{1w} adjusts the slope. The main point is that plausible, small values of H_w, C_{1w} can roughly explain the vertical dominance intermittency behaviour. The mean value $\Delta H'_t$ of about 0.05 suggests that $H'_t \approx 0.66 + 0.05 \approx 0.71$ is a better estimate. The difference with the previous estimates is because we have used only two of the three relevant datasets. (The Langley0807 dataset was excluded from the analysis since it does not provide a wide enough range of q values for which $\xi_\tau(q)$ versus $\xi_\mathrm{v}(q)$ is linear.)

5. Conclusions

In part I of this series, we proposed an anisotropic turbulence/wave model for the horizontal velocity and passive scalar fields. The model was an anisotropic, space–time, multifractal extension of the classical Kolmogorov and Corrsin–Obukhov laws – a turbulence/wave extension of the classical Fractionally Integrated Flux model. In part II, we considered the spatial part of the turbulent processes concentrating on the vertical stratification, surveying the literature (which we argued was compatible with the new model), and also using airborne lidar data to get crucial vertical cross-section information. This led directly to the precise estimate for the elliptical dimension of the spatial structures: $D_s = 2.55 \pm 0.02$, which eliminates the main competing theories of stratification

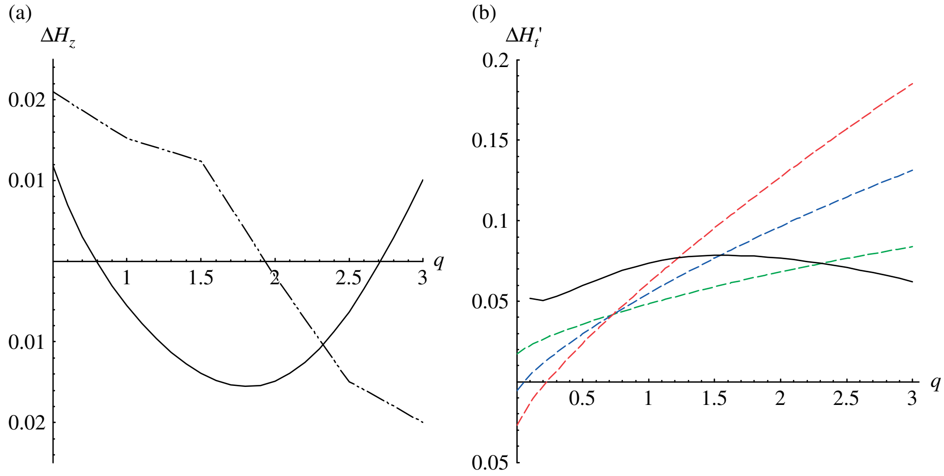

Figure 17. Intermittency corrections for stratification exponents. (a) ΔH_z averaged over three cases of horizontal wind domination (solid), and over nine vertical–horizontal cross-sections (dash dot dot); (*b*) $\Delta H_t'$ averaged over two cases of vertical wind domination (excluding Langley0807, solid) and theoretical curves (dashed), calculated with Equations (22) and (23) using parameters $\alpha_w = 1.8$, $H_w = -0.13$ and $C_{1w} = 0.013$, 0.025 and 0.038 from shallow to steep. This figure is available in colour online at www.interscience.wiley.com/qj

(with $D_s = 2$, 7/3, 3). We also found a small systematic q – or equivalently intensity – variation of about the same magnitude (0.02).

In this paper, we focused on the temporal behaviour, primarily the space–time stratification, but also the intermittency. The temporal scaling is more complex than the pure horizontal or vertical scaling treated in part II due to the effect of advection which leads to non-diagonal generators **G**. The consequences for (1-D) time series is that there are in general three competing scalings with exponents $H = 1/3$, $3/5$, $1/2$ (corresponding to $\beta_\tau = 5/3$, $11/5$, 2). The first two correspond to domination by horizontal and vertical advection, the third to 'pure' temporal development. Surveying the literature, we again found support for the theory since many studies found β_τ in the range 5/3 to 2. (In addition, the main gravity wave theories agree about this.)

While the 5/3 value poses no special problem, the other two values have difficulties. First, the vertical dominance value 11/5 has apparently never been observed, but this is not surprising in view of the fact that, unlike the horizontal wind (which typically has a large mean which may not vary much even over large space–time regions), the vertical velocity typically averages to a value near zero as we average over larger and larger regions. Indeed, this is the expected behaviour if, unlike the horizontal wind (which has $H_\mathrm{h} = 1/3$ in the horizontal), its corresponding H_w parameter is likely to be negative. On the other hand, concerning the value $\beta_\tau = 2$, an argument of Tennekes shows that, for times less than the eddy turnover time of the largest eddies (in the atmosphere, about 2 weeks), the large eddies will 'sweep' the small eddies past any fixed point so that the pure temporal development will not be observed. We therefore used meteorological analyses to directly estimate the relative importance of the various terms in the temporal scale function. The result not only confirmed Tennekes argument (although nuancing it with the consequences of intermittency), but also simultaneously showed that the vertical velocity term could occasionally dominate the horizontal velocity term. This is especially the case if the temporal scaling of the vertical velocity is taken into account. In this case we found that the effective temporal exponent decreased the naïve vertical exponent value $\beta_\tau = 11/5$ to around the (occasionally) observed value $\beta_\tau = 2$, while simultaneously increasing its probability of occurrence enough to make it quite possible that it was indeed observed in our summer data.

In sections 3, 4, we again used lidar data – although this time of both aerosol and cirrus clouds – from six ground-based lidar vertical–time cross-sections. We first confirmed the theoretical predictions in orthogonal (z, t) directions, finding the vertical scaling to be very close to the theoretical prediction ($\beta_\tau \approx 11/5$), while in the horizontal we found the two values $\beta_\tau \approx 5/3$, $\beta_\tau \approx 2$ each for three cases which – given the discussion above – we interpreted as horizontal and vertical dominance respectively.

In order to test the theory more generally (in non-orthogonal directions) and to more fully determine the physical scale function (the existence of which is the basic hypothesis of the FIF model), we developed a new Anisotropic Scaling Analysis Technique (ASAT). We compared the theoretically predicted behaviour to the data and showed good agreement between theory and experimental results over a wide range of space–time scales. As far as we could tell, the scaling of the cirrus clouds and aerosols were the same; they both followed the theoretical predictions of the turbulence/wave 23/9-D space–time model.

In its simplest form, the 23/9-D model introduces a unique anisotropic physical scale function to replace standard isotropic scales. If this function is identical – for both weak and strong structures – then the anisotropies of the weak and strong structures are the same, hence there will be constant ratios for structure function exponents in orthogonal directions. However the scale function is in fact the consequence of highly turbulent and intermittent flux dynamics, so that it would be quite surprising that there were no systematic variations of anisotropy with level of intermittency (conveniently parametrized by the order of moment q). However, in part II we found that for the vertical stratification, for mean ($q = 1$) the ratio $\xi_h/\xi_v = 0.55 \pm 0.02$, with only a very small variation with intensity, q; we estimated that the H_z was in the range 0.53 to 0.57 for most of the significant range (q decreasing from 5 to 0). For the space–time stratification investigated here, we had to consider the two cases: horizontal and vertical wind domination. For the horizontal-wind-dominated cases, we find for $q = 1$ the ratio $H_t = \xi_\tau/\xi_v = H_z = 0.54 \pm 0.02$ (theory predicts $H_z = 5/9$) and for the vertical-wind-domination case, we found the corresponding ratio $\xi_\tau/\xi_v = 0.81 \pm 0.04$. (In each case, the spread is the realization to realization variability). Assuming $H_z = 5/9$, this implies the corresponding $H'_t = \xi_\tau/\xi_h = (5/9)(0.81 \pm 0.04) = 0.68 \pm 0.03$. In order to check for systematic variations with q, we considered the ensemble-averaged structure functions and found a fairly constant values of about $H_t = 0.54$ and $H'_t = 0.71$ respectively with variations of the order 0.02 over the range $0 < q < 3$, i.e. the theory is well respected, although for the vertical-wind-dominated cases there is not a precise theoretical prediction.

If the analyses and models discussed in this series of papers are correct in their essentials, then atmospheric dynamics are in many ways simpler than usually assumed, primarily because the 23/9-D model unifies the dynamics over the entire dynamically significant range of space–time scales. Theoretically, this is compatible – if not demanded – by the dynamical equations which are scaling from planetary down to dissipation scales. On the contrary, all the competing models require the existence of scale separations with the small and large scales interacting only weakly. This is true not only of the classical 2-D/3-D isotropic turbulence model, but also of the anisotropic gravity wave models which require a linearization of the dynamics about an ill-defined reference state. The failure of modern data to corroborate the existence of a scale separation is probably the single most compelling argument in favour of the anisotropic scaling model; in this series, state-of-the-art lidar data quantitatively support the 23/9-D model while excluding the competing 2-D, 3-D and 7/3-D (gravity wave) models. Work in progress (by some of the authors and J. Stolle) shows that some general circulation models also respect wide-range space–time scaling (with a cascade structure) and so these results are probably at least roughly compatible with numerical models of the atmosphere. Finally, there has been particular ambiguity about the temporal scaling properties; the finding here that one may expect either the horizontal or vertical wind to dominate with corresponding different exponents may finally allow a deeper understanding of the evolution of meteorological systems. It may be that the distinction between horizontal- and vertical-dominated systems provides a quantitative basis for the current phenomenological distinction between convective and stratiform systems.

Acknowledgements

The authors would like to acknowledge the Meteorological Service of Canada for the Pacific 2001 and CARE 2003 experiments. The authors also acknowledge the Center for Atmospheric Research Experiments for the close collaboration during this project and in particular the support of M. Travis. Shaun Lovejoy and Alexander Radkevich acknowledge the Canadian Foundation for Climate and Atmospheric Sciences for financial support.

References

Balsley BB, Carter DA. 1982. The spectrum of atmospheric velocity fluctuations at 8 km and 86 km. *Geophys. Res. Lett.* **9**: 465–468.

Balsley BB, Garello R. 1985. The kinetic energy density in the troposphere, stratosphere and mesosphere: a preliminary study using the Poker Flat MST radar in Alaska. *Radio Sci.* **20**: 1355–1362.

Beatty TJ, Hostetler CA, Gardner CS. 1992. Lidar observation of gravity waves and their spectra near the mesopause and stratopause at Arecibo. *J. Atmos. Sci.* **49**: 477–496.

Comte-Bellot G, Corrsin S. 1971. Simple Eulerian time correlation of full- and narrow-band velocity signals in grid generated, isotropic turbulence. *J. Fluid. Mech.* **48**: 273–337.

Fritts DC, Tsuda T, VanZandt TE, Smith SA, Sato T, Fukao S, Kato S. 1990. Studies of velocity fluctuations in the lower atmosphere using MU radar. Part II: Momentum flux and energy densities. *J. Atmos. Sci.* **47**: 51–66.

Gagnon JS, Lovejoy S, Schertzer D. 2006. Multifractal earth topography. *Nonlin. Processes Geophys.* **13**: 541–570.

Gardner CS, Voelz DG. 1987. Lidar studies of the nighttime sodium layer over Urbana, Illinois. 2: Gravity waves. *J. Geophys. Res.* **92**: 4673–4694.

Hwang HJ. 1970. Power density spectrum of surface wind speed on Palmyra Island. *Mon. Weather Rev.* **98**: 70–74.

Inoue E. 1951. On the turbulent diffusion in the atmosphere. *J. Meteorol. Soc. Japan* **29**: 32.

Kwon KH, Gardner CS, Avery SK, Avery JP. 1990. Correlative radar and sodium lidar observation of the vertical and horizontal structure of gravity waves near the mesopause. *J. Geophys. Res.* **95**: 13737–13748.

Landau LD, Lifshitz EM. 1959. *Fluid Mechanics.* Pergamon: London.

Larsen MF, Kelly MC, Gage KS. 1982. Turbulence spectra in the upper troposphere at periods between 2 hours and 40 days. *J. Atmos. Sci.* **39**: 1035–1041.

Lilley M, Lovejoy S, Strawbridge KB, Schertzer D. 2004. 23/9-dimensional anisotropic scaling of passive admixtures using lidar aerosol data. *Phys. Rev. E* **70**: 036307.

Lilley M, Lovejoy S, Strawbridge KB, Schertzer D, Radkevich A. 2008. Scaling turbulent atmospheric stratification. II: Spatial stratification and intermittency from lidar data. *Q. J. R. Meteorol. Soc.* **134**: in press.

Lovejoy S, Hovde S, Tuck AF, Schertzer D. 2007. Is isotropic turbulence relevant in the atmosphere? *Geophys. Res. Lett.* **34**: L14802, DOI: 10.1029/2007GL029359.

Lovejoy S, Schertzer D. 2007. Scale, scaling and multifractals in geophysics: twenty years on. In *Nonlinear dynamics in geosciences*, Elsner J, Tsonis A (Eds.). Springer: New York, 311–337.

Mandelbrot BB. 1974. Intermittent turbulence in self-similar cascades: Divergence of high moments and dimension of the carrier. *J. Fluid Mech.* **62**: 331–350.

Meek CE, Reid IM, Manson AH. 1985. Observations of mesospheric wind velocities. 2: Cross sections of power spectral density for 48–8 hours, 8–1 hours, and 1 hour to 10 min over 60–110 km for 1981. *Radio Sci.* **20**: 1363–1382.

Radkevich A, Lovejoy S, Strawbridge KB, Schertzer D. 2007. The elliptical dimension of space-time atmospheric stratification of passive admixtures using lidar data. *Physica A* **382**: 597–615.

Scheffler AO, Liu CH. 1985. On observation of gravity wave spectra in the atmosphere using MST radar. *Radio Sci.* **20**: 1309–1322.

Schertzer D, Lovejoy S. 1985. The dimension and intermittency of atmospheric dynamics. Pp. 7–33 in *Turbulent Shear Flow 4* Launder B. (ed.) Springer-Verlag.

Schertzer D, Lovejoy S. 1987. Physical modeling and analysis of rain and clouds by anisotropic scaling of multiplicative processes. *J. Geophys. Res.* **92**: 9693–9714.

Shlien DJ, Corrsin S. 1974. A measurement of Lagrangian velocity autocorrelation in approximately isotropic turbulence. *J. Fluid. Mech.* **62**: 255–271.

Sica RJ, Russell AT. 1999. Measurements of the effects of gravity waves in the middle atmosphere using parametric models of density fluctuations. Part I: Vertical wavenumber and temporal spectra. *J. Atmos. Sci.* **56**: 1308–1329.

Strawbridge KB, Snyder BJ. 2004. Planetary boundary-layer height determination during Pacific 2001 using the advantage of a scanning lidar instrument. *Atmos. Environ.* **38**(34): 5861–5871.

Taylor GI. 1938. The spectrum of turbulence. *Proc. R. Soc. London A* **164**: 476–490.

Tennekes H. 1975. Eulerian and Lagrangian time microscales in isotropic turbulence. *J. Fluid. Mech.* **67**: 561–567.